





Testing wave turbulence theory for the Gross-Pitaevskii system

Ying Zhu ^{1,*}, Boris Semisalov ^{2,3,4}, Giorgio Krstulovic ² and Sergey Nazarenko ¹

¹*Université Côte d'Azur, CNRS, Institut de Physique de Nice (INPHYNI), Parc Valrose, 06108 Nice, France*

²*Université Côte d'Azur, Observatoire de la Côte d'Azur, CNRS, Laboratoire Lagrange, Boulevard de l'Observatoire CS 34229 – F 06304 Nice Cedex 4, France*

³*Novosibirsk State University, 1 Pirogova street, 630090 Novosibirsk, Russia*

⁴*Sobolev Institute of Mathematics SB RAS, 4 Academician Koptyug Avenue, 630090 Novosibirsk, Russia*



(Received 14 December 2021; accepted 4 May 2022; published 8 July 2022)

We test the predictions of the theory of weak wave turbulence by performing numerical simulations of the Gross-Pitaevskii equation (GPE) and the associated wave-kinetic equation (WKE). We consider an initial state localized in Fourier space, and we confront the solutions of the WKE obtained numerically with GPE data for both the wave-action spectrum and the probability density functions (PDFs) of the Fourier mode intensities. We find that the temporal evolution of the GPE data is accurately predicted by the WKE, with no adjustable parameters, for about two nonlinear kinetic times. Qualitative agreement between the GPE and the WKE persists also for longer times with some quantitative deviations that may be attributed to the combination of a breakdown of the theoretical assumptions underlying the WKE as well as numerical issues. Furthermore, we study how the wave statistics evolves toward Gaussianity in a timescale of the order of the kinetic time. The excellent agreement between direct numerical simulations of the GPE and the WKE provides a solid foundation to the theory of weak wave turbulence.

DOI: [10.1103/PhysRevE.106.014205](https://doi.org/10.1103/PhysRevE.106.014205)

I. INTRODUCTION

Wave turbulence (WT) is a state of a continuous medium characterized by the presence of random mutually interacting waves with a broadband spectrum [1–3]. Weak WT theory is a mathematical framework describing the statistical behavior of WT dominated by weakly nonlinear waves. The main object in this theory is the wave-action spectrum, which is the second-order moment of the wave amplitude and which evolves according to the so-called wave-kinetic equation (WKE). Special attention in past literature was given to studies of stationary scaling solutions of this equation, which are similar to the Kolmogorov spectrum of hydrodynamic turbulence, the so-called Kolmogorov-Zakharov (KZ) spectra (see, e.g., [4–7]). However, nonstationary WT is also interesting because it is often characterized by mathematically nontrivial solutions exhibiting self-similar asymptotic behavior [8–13]. In general, nonstationary WT allows more subtle tests of the weak WT theory than stationary setups, which is why we will consider it in the present paper. Further, the weak WT theory can be also extended to describing the higher-order moments and even to the full joint probability density function (PDF) of the wave intensities [1,14–17]. The fundamental concepts of WT were laid out in Ref. [2]. An introduction to WT as well as a summary of recent developments in this area can be found in Ref. [1]. Reference [18] contains a collection of reviews about recent experiments in WT.

Over the past few years, a significant push was made in the direction of rigorous mathematical justification of the weak WT theory. The state-of-the-art result is a claim made in [19] that the WKE (9) derived from the three-dimensional (3D) Gross-Pitaevskii equation (GPE) (1) truthfully predicts the evolution of the wave spectrum (under certain requirements of the initial conditions) up to a time δT_{kin} , where T_{kin} is the characteristic evolution time of the WKE, and $\delta \ll 1$. This result is significant from a mathematical point of view because δ is independent of the (vanishing) nonlinearity strength and the (expanding to infinity) physical size of the system. As such, this result is the wave analog of the famous Lanford's theorem on the Boltzmann kinetic equation from colliding particle systems. However, this result is insufficient for physical applications, in the majority of which one is interested in evolution at times $\gtrsim T_{\text{kin}}$ when the spectrum has significantly evolved away from its initial shape, whereas at time δT_{kin} it is still very close to the initial one.

Thus, the main motivation of the present study is to test weak WT theory at times $\gtrsim T_{\text{kin}}$ by juxtaposition of the spectra arising from the direct numerical simulations (DNSs) of the 3D GPE (1) and from the simulations of the WKE (9). Further, we explore numerically the evolution of the wave-intensity PDFs and the statistical quantities associated with them, e.g., the cumulants. We show that both the spectra and the PDFs for the WKE and the GPE agree with each other very well for times $\gtrsim T_{\text{kin}}$, and we characterize the departures at later times.

The first comparisons for the spectra, PDFs, and cumulants obtained from a DNS and simulations of the weak WT closure can be found in [20] for a model 2D three-wave system (using simulations up to $\sim 0.3T_{\text{kin}}$). They arrived at favorable

*yzhu@unice.fr

conclusions for the validity of the weak WT theory. The system considered in the present work is 3D and four-wave, and our simulations extend to about $10T_{\text{kin}}$. In addition, in the present work we take advantage of the analytical expression for the PDF in terms of the wave spectrum, which was obtained in [21] and, therefore, was not known at the time of writing Ref. [20].

Further, a comparison of the evolving spectra arising in the numerics of WKE and the original dynamic model was also done in [22,23] for deep water surface gravity waves. That study was oriented on the practical problem of sea swell modeling, with comparisons made on a qualitative level by visually comparing the plots. Further modifications by introducing dissipation and forcing were explored with a view to make the models more realistic for practical modeling of the sea waves [24]. In contrast, our study is aimed at the more fundamental aspects of the weak WT theory validity rather than a particular real life wave phenomenon. To make the comparisons equivalent, we do not introduce any extra terms to improve the modeling. We introduce global measures characterizing the spectra, such as the energy and the wave-action centroids, to make our comparisons more quantitative. Finally, note that the recent work in [25] compares the evolution of the one-dimensional defocusing quintic nonlinear Schrödinger equation with the evolution of the associated WKE, finding good agreement when some scaling relations between nonlinearity strength and system size are fulfilled.

The present paper is organized as follows. In Sec. II we introduce the GPE and the setting we consider in this work. We provide then a short introduction to the theory of weak wave turbulence, and we present the wave-kinetic equation. The dynamics of the probability distribution functions of the wave-action spectra is also discussed. In Sec. III, we explain our numerical methods for integrating the GPE and the WKE. Then, in Sec. IV we present our numerical results, where we directly compare numerical simulations of the GPE and the WKE. Finally, in Sec. V we present our conclusions. We present the details on the derivation of the WKE in an isotropic homogeneous setup to the Appendix A and discuss the most important issues of the new numerical algorithm used for solving WKE in Appendix B.

II. THEORETICAL BACKGROUND

A. Gross-Pitaevskii equation

The dimensionless Gross-Pitaevskii equation (GPE) in a 3D physical space $\mathbf{r} = \{x, y, z\}$ for the complex wave function $\psi(\mathbf{r}, t)$ is

$$i \frac{\partial \psi(\mathbf{r}, t)}{\partial t} = [-\nabla^2 + |\psi(\mathbf{r}, t)|^2] \psi(\mathbf{r}, t). \quad (1)$$

The GPE is also known as the defocusing nonlinear Schrödinger equation (NLSE). This equation describes the dynamics of Bose-Einstein condensates (BEC) [26], nonlinear light [3], and other important physical systems, and as such it is a universal master equation that allows us to study fundamental nonlinear phenomena including nonlinear wave interactions. Consider the nonlinear wave system described by the GPE (1) in the L -periodic box of volume $V = L^3$. From GPE (1) we have the following Hamiltonian equations for the

Fourier coefficients of the wave function:

$$i \dot{a}_{\mathbf{k}} = \frac{\partial \mathcal{H}}{\partial a_{\mathbf{k}}^*},$$

$$\mathcal{H} = \sum_{\mathbf{k}} \omega_{\mathbf{k}} |a_{\mathbf{k}}|^2 + \frac{1}{2} \sum_{\mathbf{k}_1, \mathbf{k}_2, \mathbf{k}_3, \mathbf{k}_4} a_{\mathbf{k}_1}^* a_{\mathbf{k}_2}^* a_{\mathbf{k}_3} a_{\mathbf{k}_4} \delta_{12}^{34}, \quad (2)$$

where $\mathbf{k}, \mathbf{k}_1, \mathbf{k}_2, \mathbf{k}_3, \mathbf{k}_4 \in \frac{2\pi}{L} \mathbb{Z}^3$ are the wave vectors, $\omega_{\mathbf{k}} = k^2$ is the frequency of the linear wave with wave vector \mathbf{k} , $k = |\mathbf{k}|$, and $a_{\mathbf{k}} \in \mathbb{C}$ is the wave-action variable:

$$a_{\mathbf{k}} = \hat{\psi}_{\mathbf{k}} = \frac{1}{V} \int \psi(\mathbf{r}, t) e^{-i\mathbf{k}\cdot\mathbf{r}} d\mathbf{r}, \quad (3)$$

$\delta_{12}^{34} = \delta(\mathbf{k}_1 + \mathbf{k}_2 - \mathbf{k}_3 - \mathbf{k}_4)$, and the integral is taken over all the possible discrete values of $\mathbf{k}_1, \mathbf{k}_2, \mathbf{k}_3$, and \mathbf{k}_4 .

The GPE (1) conserves the mean density of particles,

$$N = \frac{1}{V} \int |\psi(\mathbf{x}, t)|^2 d\mathbf{x}, \quad (4)$$

and the mean density of energy,

$$H = \frac{1}{V} \int \left[|\nabla \psi(\mathbf{x}, t)|^2 + \frac{1}{2} |\psi(\mathbf{x}, t)|^4 \right] d\mathbf{x}. \quad (5)$$

The total energy density can be split into two parts—the energy density of the linear-dynamics $H_2 = \frac{1}{V} \int |\nabla \psi(\mathbf{x}, t)|^2 d\mathbf{x}$, and the nonlinear-dynamics energy $H_4 = \frac{1}{V} \int \frac{1}{2} |\psi(\mathbf{x}, t)|^4 d\mathbf{x}$. In a wave-turbulent state, the total energy and the density of particles cascade in opposite directions [1,3], which is similar to the dual cascade behavior in 2D hydrodynamic turbulence [27].

An important quantity, which characterizes the system, is the healing length, $\xi = \frac{1}{\sqrt{N}}$, which refers to an average scale at which the nonlinear term becomes comparable with the linear one. The characteristic wave number corresponding to ξ is defined as $k_{\xi} = \frac{1}{\xi}$.

Also, we define the condensate fraction as

$$C_0 = \frac{|\hat{\psi}_0|^2}{N}. \quad (6)$$

$C_0 = 0$ means that there is no homogeneous condensate in the field, and $C_0 = 1$ represents a complete condensation. When the condensate fraction is small or absent, and the waves are weak, the system described by the GPE can be modeled within the weak WT approach leading to the four-wave WKE [1] introduced in the next subsection.

B. Wave-kinetic equation description

The analysis of the GPE in the case of weak nonlinearity leads to the integrodifferential WKE describing the evolution of the wave-action spectrum,

$$n_{\mathbf{k}}(t) = n(\mathbf{k}, t) = \left(\frac{L}{2\pi} \right)^3 \langle |a_{\mathbf{k}}|^2 \rangle, \quad (7)$$

where the angular brackets denote averaging over the ensemble of initial conditions.

To make all further considerations consistent with the weak WT theory, let us briefly summarize the basic steps of

derivation of the WKE from the GPE [1]:

(i) Consider the GPE in the Fourier space.

(ii) Set a small parameter $0 < \varepsilon \ll 1$, which is the measure of nonlinearity, and consider the GPE on the intermediate timescale T_I between the linear and nonlinear timescales:

$$\frac{2\pi}{k^2}(\text{linear scale}) \ll T_I \sim \frac{2\pi}{\varepsilon k^2} \ll \frac{2\pi}{\varepsilon^2 k^2}(\text{nonlinear scale}).$$

(iii) Introduce the interaction representation variable,

$$\hat{b}_{\mathbf{k}}(t) = \frac{1}{\sqrt{\varepsilon}} \hat{\psi}_{\mathbf{k}} \exp(i\tilde{\omega}_{\mathbf{k}}t), \quad \tilde{\omega}_{\mathbf{k}} = k^2 + 2N. \quad (8)$$

Here, the second term in $\tilde{\omega}_{\mathbf{k}}$ is the so-called nonlinear frequency shift: it is the leading-order nonlinear effect, but it does not lead to energy exchanges between the Fourier modes.

(iv) Assume that initially the amplitudes $|\hat{b}_{\mathbf{k}}|$ and the phase factors $\hat{b}_{\mathbf{k}}/|\hat{b}_{\mathbf{k}}|$ are statistically independent random variables, and the phase factors are uniformly distributed on the unit

circle in the complex plane. This was called the random phase and amplitude (RPA) statistics in [15–17], which is a change to the standard meaning of this acronym “random phase approximation” made in order to emphasize that the amplitude randomness is essential for the WT closure and the fact that there is no approximation involved in taking initial conditions of this type.

(v) Make the asymptotic expansion of $\hat{b}_{\mathbf{k}}(T_I)$ with respect to the small parameter ε , substitute it into the GPE, and find the averaged coefficients with the aid of the RPA property.

(vi) Approximate the time derivative of the wave-action spectrum by a difference quotient, express it through the obtained averaged coefficients, and pass first to the large box limit $L \rightarrow \infty$ (which makes the k -space continuous). Then pass to the limit $T_I \rightarrow \infty$.

As a result, one obtains the following WKE for the four-wave interaction $\mathbf{k}, \mathbf{k}_1 \rightarrow \mathbf{k}_2, \mathbf{k}_3$ [28]:

$$\frac{d}{dt}n_{\mathbf{k}} = 4\pi \int \delta(\mathbf{k} + \mathbf{k}_1 - \mathbf{k}_2 - \mathbf{k}_3)\delta(\omega_{\mathbf{k}} + \omega_{\mathbf{k}_1} - \omega_{\mathbf{k}_2} - \omega_{\mathbf{k}_3})[n_{\mathbf{k}_1}n_{\mathbf{k}_2}n_{\mathbf{k}_3} + n_{\mathbf{k}}(n_{\mathbf{k}_2}n_{\mathbf{k}_3} - n_{\mathbf{k}_1}n_{\mathbf{k}_3} - n_{\mathbf{k}_1}n_{\mathbf{k}_2})]d\mathbf{k}_1d\mathbf{k}_2d\mathbf{k}_3, \quad (9)$$

where δ is the Dirac δ -function, and wave vectors are now continuous ($\mathbf{k}_i \in \mathbb{R}^3$).

The collision integral on the right-hand side (RHS) of (9) is taken over a nine-dimensional space. However, we shall consider the situation when the wave fields are isotropic. In this situation, averaging over directions reduces considerably the dimension of integration. Such a simplification makes it possible to study complex nonstationary self-similar solutions of the second kind; see, for instance, [8–10,13,29]. Performing the angle averaging leads to a new collision kernel. Previous results presented in the literature reported disparate prefactors of the kernel [2,8,30]. The value of this prefactor is crucial for a quantitative comparison of the evolution of GPE and WKE solutions. In Appendix A, we provide a careful derivation, where we have corrected previous errors.

Assuming the isotropy, we consider the wave-action spectrum that depends only on $k = |\mathbf{k}|$ and we pass to the frequency variable: $n_{\mathbf{k}}(t) = n_{\omega}(t) = n(\omega, t)$, where $\omega = k^2$ is the new variable. The isotropic WKE is

$$\frac{d}{dt}n_{\omega} = \frac{4\pi^3}{\sqrt{\omega}} \int S(\omega, \omega_1, \omega_2, \omega_3)\delta_{1\omega}^{23}n_{\omega}n_1n_2n_3 \times (n_{\omega}^{-1} + n_1^{-1} - n_2^{-1} - n_3^{-1})d\omega_1d\omega_2d\omega_3, \quad (10)$$

where $\delta_{1\omega}^{23} = \delta(\omega + \omega_1 - \omega_2 - \omega_3)$. The integral on the RHS of (10) is taken over all positive values of $\omega_1, \omega_2, \omega_3$. The kernel of the integral is

$$S(\omega, \omega_1, \omega_2, \omega_3) = \min(\sqrt{\omega}, \sqrt{\omega_1}, \sqrt{\omega_2}, \sqrt{\omega_3}). \quad (11)$$

Making use of $\delta_{1\omega}^{23}$, and defining $n_c(t) = n(\omega_2 + \omega_3 - \omega, t)$, $S_{\omega}^{23} = S(\omega, \omega_2 + \omega_3 - \omega, \omega_2, \omega_3)$, and $\Delta_{\omega} = \{(\omega_2, \omega_3) : \omega_2, \omega_3 \geq 0, \omega_2 + \omega_3 \geq \omega\}$, one can do further simplifications of the WKE. Finally, it reduces to

$$\frac{d}{dt}n_{\omega} = \eta_{\omega}(t) - n_{\omega}(t)\gamma_{\omega}(t), \quad (12)$$

where

$$\eta_{\omega}(t) = \frac{4\pi^3}{\sqrt{\omega}} \int_{\Delta_{\omega}} S_{\omega}^{23}n_cn_2n_3d\omega_2d\omega_3, \quad (13)$$

$$\gamma_{\omega}(t) = \frac{4\pi^3}{\sqrt{\omega}} \int_{\Delta_{\omega}} S_{\omega}^{23}[n_c(n_2 + n_3) - n_2n_3]d\omega_2d\omega_3. \quad (14)$$

Equation (12) conserves the density of particles,

$$N = 2\pi \int_0^{\infty} \omega^{1/2}n_{\omega}d\omega, \quad (15)$$

and the density of linear-dynamics energy,

$$H = H_2 = 2\pi \int_0^{\infty} \omega^{3/2}n_{\omega}d\omega. \quad (16)$$

Note that in the weak WT theory, the nonlinear-dynamics energy drops out from the invariant (5). This is natural because by construction it is much smaller than the linear-dynamics energy.

Because the system we study is approximately statistically isotropic, it is natural to introduce the spherically integrated (radial) spectra of wave-action and energy defined as follows:

$$n^{\text{rad}}(k, t) = \int n_{\mathbf{k}}(t)k^2d\Omega, \quad (17)$$

$$E^{\text{rad}}(k, t) = \int n_{\mathbf{k}}(t)k^4d\Omega = k^2n^{\text{rad}}(k, t), \quad (18)$$

where $d\Omega$ is the surface element of the unit sphere in the 3D \mathbf{k} -space.

Note that $n^{\text{rad}}(k, t)$ and $E^{\text{rad}}(k, t)$ indicate the distributions of particles and energy over k ; respectively, we have the relations

$$N = \int_0^{\infty} n^{\text{rad}}(k, t)dk \quad \text{and} \quad H_2 = \int_0^{\infty} E^{\text{rad}}(k, t)dk.$$

C. Wave turbulence description beyond the spectrum

It has been widely believed that the statistics of random weakly nonlinear wave systems is close to being Gaussian. Derivation of the evolution equation for the probability distribution function (PDF) of the wave intensities presented in [16] has made it possible to examine this belief. It was shown in [16] that this equation indeed has a stationary solution corresponding to the Gaussian state, but it was also noted that the typical evolution time of the PDF is the same as that for the spectrum. Thus, for nonstationary wave systems one can expect significant deviations from the Gaussianity if the initial wave distributions are non-Gaussian. Note that non-Gaussian (usually deterministic) initial conditions for the wave intensity are typical in numerical simulations in WT. Also, there is no reason to believe that initial waves excited in natural conditions, e.g., sea waves excited by wind, should be Gaussian. Therefore, the study of the evolution of the wave statistics is important for both understanding fundamental nonlinear processes and for practical predictions such as, e.g., the wave weather forecast.

In the present paper, we shall use the full general solution for the PDF equation derived in [21] and also the expressions for the moments and cumulants of the PDF from [14]. Here, we briefly summarize the results of Refs. [14,16] and [21].

Let us consider the PDF $\mathcal{P}(s_{\mathbf{k}}, t)$ of the wave intensity $J_{\mathbf{k}} = |a_{\mathbf{k}}|^2$ defined in a standard way, namely, the probability for $J_{\mathbf{k}}$ to be in the range from $s_{\mathbf{k}}$ to $s_{\mathbf{k}} + ds_{\mathbf{k}}$ is $\mathcal{P}(s_{\mathbf{k}}, t)ds_{\mathbf{k}}$. In symbolic form,

$$\mathcal{P}(s_{\mathbf{k}}, t) = \langle \delta(s_{\mathbf{k}} - J_{\mathbf{k}}) \rangle. \quad (19)$$

Under the same assumptions of the RPA and weak nonlinearity as the ones used for WKE derivation, the following evolution equation for $\mathcal{P}(s_{\mathbf{k}}, t)$ was derived in [16]:

$$\frac{\partial \mathcal{P}(s_{\mathbf{k}}, t)}{\partial t} + \frac{\partial F}{\partial s_{\mathbf{k}}} = 0, \quad (20)$$

where

$$F = -s_{\mathbf{k}} \left(\gamma_{\mathbf{k}} \mathcal{P} + \eta_{\mathbf{k}} \frac{\partial \mathcal{P}}{\partial s_{\mathbf{k}}} \right) \quad (21)$$

and, for the four-wave systems arising from the GPE,

$$\eta_{\mathbf{k}}(t) = 4\pi \int \delta(\mathbf{k} + \mathbf{k}_1 - \mathbf{k}_2 - \mathbf{k}_3) \delta(\omega_{\mathbf{k}} + \omega_{\mathbf{k}_1} - \omega_{\mathbf{k}_2} - \omega_{\mathbf{k}_3}) n_{\mathbf{k}_1} n_{\mathbf{k}_2} n_{\mathbf{k}_3} d\mathbf{k}_1 d\mathbf{k}_2 d\mathbf{k}_3, \quad (22)$$

$$\gamma_{\mathbf{k}}(t) = 8\pi \int \delta(\mathbf{k} + \mathbf{k}_1 - \mathbf{k}_2 - \mathbf{k}_3) \delta(\omega_{\mathbf{k}} + \omega_{\mathbf{k}_1} - \omega_{\mathbf{k}_2} - \omega_{\mathbf{k}_3}) \times [n_{\mathbf{k}_1} (n_{\mathbf{k}_2} + n_{\mathbf{k}_3}) - n_{\mathbf{k}_2} n_{\mathbf{k}_3}] d\mathbf{k}_1 d\mathbf{k}_2 d\mathbf{k}_3. \quad (23)$$

Note that in terms of $\eta_{\mathbf{k}}$ and $\gamma_{\mathbf{k}}$, the WKE (9) reads $\frac{d}{dt} n_{\mathbf{k}} = \eta_{\mathbf{k}} - \gamma_{\mathbf{k}} n_{\mathbf{k}}$. In the isotropic case, $\eta_{\mathbf{k}} = \eta_{\omega}$ and $\gamma_{\mathbf{k}} = \gamma_{\omega}$ as defined in (13) and (14).

It is important to realize that generally the PDF evolves at the same timescale τ_{kin} as the spectrum, namely $\tau_{\text{kin}} \sim \min(1/\gamma, n/\eta)$. The cases in which either the spectrum is close to a stationary one (e.g., the KZ spectrum) or the PDF is close to the stationary one (corresponding to the Gaussian wave fields) are exceptional. In the former case, the spectrum

evolution time becomes very large, but not necessarily the PDF evolution time, and in the latter case the opposite is true.

Laplace transform of Eq. (20) converts it into a first-order partial differential equation (PDE), which can be solved by the method of characteristics. Moreover, this PDE is linear with respect to \mathcal{P} if we consider the spectrum $n_{\mathbf{k}}(t)$ given (i.e., found by solving the WKE first). These facts were used in [21], and the general time-dependent solution of Eq. (20) for the PDF is obtained there for arbitrary initial statistics.

The solution is constructed at a fixed wave number, so we shall drop the subscripts \mathbf{k} for simplicity. Let us introduce the Green's function $\mathcal{P}_J(s, t)$, i.e., the solution evolving from the initial condition $\mathcal{P}(s, 0) = \delta(s - J)$, which corresponds to the deterministic initial wave intensity. The general solution with an arbitrary initial condition $\mathcal{P}(s, t)$ is thus given by

$$\mathcal{P}(s, t) = \int_0^{\infty} \mathcal{P}(J, 0) \mathcal{P}_J(s, t) dJ. \quad (24)$$

Using the Laplace transform and the method of characteristics, the following solution was obtained in [21]:

$$\begin{aligned} \mathcal{P}_J(s, t) &= \frac{e^{-\frac{s}{\tilde{n}} - a\tilde{n}}}{2\pi i\tilde{n}} \lim_{T \rightarrow +\infty} \int_{T-i\infty}^{T+i\infty} \frac{e^{s\rho + \frac{a}{\rho}}}{\rho} d\rho \\ &= \frac{1}{\tilde{n}} e^{-\frac{s}{\tilde{n}} - a\tilde{n}} I_0(2\sqrt{as}), \end{aligned} \quad (25)$$

where

$$\tilde{n} = n(t) - J e^{-\int_0^t \gamma(t') dt'}, \quad (26)$$

$n(0) = J$, $a = \frac{J}{\tilde{n}^2} e^{-\int_0^t \gamma(t') dt'}$, and $I_0(x)$ is the zeroth modified Bessel function of the first kind.

This is a general solution for an arbitrary initial PDF, but we emphasize that $n(t)$ is considered given. Thus, finding the PDF is a two-step process: first, one has to find $n_{\mathbf{k}}(t)$ by solving the WKE (usually numerically), and second, one must substitute the result into the above formula for the analytical solution.

Note that for Gaussian wave fields, the PDF of the wave intensities is $\mathcal{P}_G = \frac{1}{n} e^{-s/n}$. As shown in [21], solutions (24) and (25) imply that (a) the fields, which are Gaussian initially, will remain Gaussian for all time, and (b) at each fixed s wave turbulence asymptotically becomes Gaussian if

$$\lim_{t \rightarrow \infty} \frac{n(0) e^{-\int_0^t \gamma(t') dt'}}{n(t)} = 0. \quad (27)$$

Indeed, taking into account that $I_0(0) = 1$, we recover that $\mathcal{P}_J \rightarrow \mathcal{P}_G = \frac{1}{n} e^{-s/n}$ as $t \rightarrow \infty$ if condition (27) is satisfied provided that $as \ll 1$. Notice also that $a(t) \rightarrow 0$.

It is interesting that the rate of convergence to Gaussianity is greater at those k 's where the initial spectrum is smaller. Indeed, in the limit $J = n(0) \rightarrow 0$ we have $\tilde{n} \rightarrow n$ and $a \rightarrow 0$, so that $\mathcal{P}_J \rightarrow \mathcal{P}_G = \frac{1}{n} e^{-s/n}$.

On the other hand, for large t and $as \gg 1$, taking into account that $I_0(x) \xrightarrow{x \rightarrow \infty} \frac{e^x}{\sqrt{2\pi x}}$, we have

$$\mathcal{P}_J(s, t) \rightarrow \frac{\mathcal{P}_G}{(2\pi)^{1/2} (as)^{1/4}} e^{2\sqrt{as} - as} \ll \mathcal{P}_G. \quad (28)$$

Thus, there is a front at $s \sim s^*(t) = 1/a$ moving toward large s as $t \rightarrow \infty$. The PDF ahead of this front is depleted with

respect to the Gaussian distribution, whereas behind the front it is asymptotically approaching Gaussianity. Similar behavior will be realized for any solution (24) evolving from an initial PDF whose decay at large s is faster than exponential.

Further, we shall also consider the moments

$$M^{(p)} = \langle |a|^{2p} \rangle \quad (p = 1, 2, 3, \dots),$$

so that the spectrum $n_{\mathbf{k}}$ is represented by the first moment ($p = 1$), whereas the higher moments contain information about fluctuations of the wave-action spectrum about its mean value. For example, for the standard deviation, we have

$$\sigma = (\langle |a|^4 \rangle - \langle |a|^2 \rangle^2)^{1/2} = [M^{(2)} - (M^{(1)})^2]^{1/2}. \quad (29)$$

If the wave amplitudes are deterministic, then $M^{(p)} = (M^{(1)})^p$ and $\sigma = 0$. For the opposite extreme of large fluctuations, we would have $M^{(p)} \gg (M^{(1)})^p$, which means that the typical realization is sparse in the k -space and is characterized by few intermittent peaks.

For Gaussian fields, $M^{(p)} = p! (M^{(1)})^p$. To study the deviations from Gaussianity, it is useful to look at the relative cumulants

$$F^{(p)} = \frac{M^{(p)} - p! (M^{(1)})^p}{p! (M^{(1)})^p}, \quad p = 1, 2, 3, \dots \quad (30)$$

By definition, $F^{(1)}$ is always zero. For $p = 2$, this expression measures the flatness of the distribution of Fourier amplitudes at each k . It determines the rms of the fluctuations of the wave-action $\sigma^2 = M^{(2)} - (M^{(1)})^2 = (M^{(1)})^2(2F^{(2)} + 1)$.

The general solution for the relative cumulants can be obtained either from the general solution for the PDF, (24), (25), or by direct derivation of these quantities using the weak WT turbulence, as was done in [14]. The result is

$$F^{(p)}(t) = e^{-p\theta} \sum_{j=2}^p \frac{\theta^{p-j} p!}{j!(p-j)!} F^{(j)}(t=0), \quad (31)$$

where $\theta = \int_0^t \frac{\eta}{n} dt'$ is an effective time variable. One can see that expression (31) decays as $t \rightarrow \infty$ for any fixed p , provided that $\theta \rightarrow \infty$. This condition for approaching Gaussianity is equivalent to the respective condition for the PDF solution, Eq. (27).

It was noted in [14] that, even if the $F^{(p)}$ eventually decay to zero at each fixed p , their initial values propagate in p without decay toward the larger values of p . This effect is interconnected with the propagation of the PDF front toward larger s , which we discussed before.

Below, we are going to report on the numerical simulations of the GPE and the WKE, in which the predictions described above about the PDF and the relative cumulants will be put to the test alongside the comparisons of the wave spectra.

III. NUMERICAL METHODS

A. Gross-Pitaevskii equation

The GPE (1) is a partial differential equation with a cubic nonlinearity, which in the present work is considered in a 3D physical space and integrated with the pseudospectral code FROST. The complex field $\psi(\mathbf{r}, t)$ is taken to be triply periodic in the physical space with period L and represented on the grid of $N_p \times N_p \times N_p$ points. We evaluate the linear terms in

Fourier space and the nonlinear term in the physical space, which we then transform to Fourier space. The classical 2/3 rule is used for dealiasing [31]. The parallelization of the code uses the interface of MPI communication and standard fast Fourier transforms (FFTs) of the FFTW library [32]. The library distributes the computation on various processors in dividing the domain into slices. For very large resolutions, a partially hybrid scheme is implemented, in addition to the OpenMP shared memory library. This scheme allows us to use more processors at fixed resolutions. One can find more details about the FROST code in [33].

For integration on GPE with respect to the time variable, we employ the exponential time differencing Runge-Kutta scheme of fourth order (ETD4RK) (see [34]). In contrast to the classical Runge-Kutta scheme, it provides good precision of approximation for both dissipative and dispersive partial differential equations (e.g., the GPE as the latter), especially at the smallest scales of the Fourier space.

In the Fourier space, we compute the spherically integrated wave-action spectra $n^{\text{rad}}(k, t)$ defined by Eq. (17) using its discrete space version:

$$n^{\text{rad}}(k, t) = \frac{1}{D_k} \sum_{\mathbf{k} \in \Gamma_k} |\hat{\psi}(\mathbf{k}, t)|^2. \quad (32)$$

Here, Γ_k is the spherical shell around $|\mathbf{k}| = k$ with the thickness of D_k , where D_k is equal to the mesh size $2\pi/L$ (spacing between the grid points in the Fourier space). Such a spherically integrated spectrum represents the wave-action density in the 1D space of $k = |\mathbf{k}|$: it is relevant to the situations when turbulence is (at least approximately) statistically isotropic.

We run the code with resolutions $N_p = 128, 256, \text{ and } 512$ and fix the maximum $|\mathbf{k}|$ to be k_{cutoff} , so that the sizes of the periodic box are $L = 2\pi, 4\pi, \text{ and } 8\pi$, respectively. For each spatial resolution, an appropriate constant time step is set, such that the relative variation of the global invariants is less than 10^{-4} .

A comment is due on the procedure of averaging in the GPE simulations. Strictly speaking, for computing the ensemble-averaged spectrum and the PDF of $J_{\mathbf{k}}$ generated by the GPE, one should perform a large number of numerical simulations starting from independent random initial fields. Performing such a task is unrealistic because it would require computational resources that are far beyond the ones presently available. Instead of this, thanks to the approximate statistical isotropy, we get the statistical averaging via using all wave vectors contained in a given spherical shell in the spectral space. Note that the statistical isotropy is present in the initial conditions, and it is approximately preserved throughout the simulations at the small scales (where the influence of the large-scale anisotropy due to the 3D periodic cube is minimal).

B. Wave-kinetic equation

The WKE is solved numerically by adapting the method developed in [13] and by applying a second order Runge-Kutta scheme for time marching. The integrals of the collision term are computed using decomposition of the domain of integration into bounded subdomains, inside of which the integrands are highly smooth functions. Each subdomain is

mapped to the reference square, where we construct special grids. Coordinates of nodes of these grids are zeros of Chebyshev polynomials. Then, we adapt and modify the Clenshaw-Curtis quadrature to compute the integrals on such grids. This method is well suited for the collisional kernel of the GPE-based WKE, and it is highly accurate and efficient [13].

For approximating the spectra on the specified range $[\omega_{\min}, \omega_{\max}] \subset [0, \infty)$, we use a barycentric interpolation formula with Chebyshev nodes. In our study, we set $\omega_{\min} = 0.1^2$, $\omega_{\max} = 86^2$. The generalization of the barycentric formula to the class of rational approximations is used as well. Such a method enables one to resolve possible singularities of spectra. To compute the collision term we use constant continuation of the function $n_\omega(t)$ to the segment $\omega \in [0, \omega_{\min}]$, and we assume that $n_\omega(t) = 0$ for all $\omega > \omega_{\max}$ and all t . More details can be found in Appendix B.

Numerical solutions of the WKE are defined on a grid presenting a scale separation of almost six decades in ω . The time step and the space grid are adjusted in order to ensure a good conservation of invariants. To address the issue of conservation, let us recall that the solution of the WKE is predicted to blow up at $\omega = 0$ at a finite time t^* [8–10,13], which was estimated in our numerical tests as $t^* \approx 126.7$. For the times $t \in [0, 100]$, which are far from t^* , we used the grid with 128 nodes. The maximum relative deviations of the particle and energy densities from their initial values are 4.7×10^{-5} and 7.6×10^{-4} , respectively. This nonconservation is mainly due to the leak of particles and energy through the boundary ω_{\max} . To compute the spectrum at the time $t = 125.7$, which is rather close to t^* (see Fig. 6), we use a much finer grid with 1024 nodes and expand the segment $[\omega_{\min}, \omega_{\max}]$ to $[0.001, 100^2]$ in order to reduce the leak. In this case, the biggest nonconservation 3.69×10^{-4} is observed for the particle density. However, it is worth noting that this small nonconservation of the total particle number is accompanied with a rather large approximation error, of the order 15%, in the pointwise values of the wave-action spectrum in the vicinity of ω_{\min} . This error is estimated by comparing the 1024 and 512 results. This leads to the conclusion that at the moment $t = 125.7$, i.e., rather close to the blowup t^* , our method still provides an adequate description. More details are available in Appendix B.

Finally, to compare solutions of the WKE with those of the GPE, we notice that

$$n^{\text{rad}}(k, t) = 4\pi\omega n_\omega(t), \quad (33)$$

where the dispersion relation $\omega = k^2$ was used.

C. Probability distribution functions

We shall concentrate our attention on the case when the initial amplitudes are deterministic, so that the PDF is given by the Green's function $\mathcal{P}_J(t, s)$. We shall also consider the isotropic WT and examine the solutions at several different $k = |\mathbf{k}|$. Before computing $\mathcal{P}_J(t, s)$ for a given k by formula (25), it is convenient to normalize the PDF, so that the first moment of the new variable is equal to unity. Here we introduce the normalized PDF $\tilde{\mathcal{P}}_J(t, \tilde{s}) = \langle s \rangle \mathcal{P}_J(t, \tilde{s}\langle s \rangle)$ with the new stochastic variable $\tilde{s} = s/\langle s \rangle$, where $\langle s \rangle$ represents the

ensemble average of intensity $J_{\mathbf{k}}$ at time t . After this normalization, the PDF corresponding to the Gaussian statistics becomes $\mathcal{P}_G(\tilde{s}) = \exp(-\tilde{s})$.

To compute the normalized PDF $\tilde{\mathcal{P}}(t, \tilde{s})$, we first solve the WKE numerically using the algorithm described in Sec. III B, and then we use the found spectrum to compute $\mathcal{P}_J(t, s)$ using (25). To compute the temporal integral of $\gamma(t')$ in (26), we use a Gaussian quadrature formula with nine nodes. We carefully check that the PDF is properly normalized, and the mean of \tilde{s} is 1 up to an error smaller than 3×10^{-4} .

IV. NUMERICAL RESULTS

The simulations of both GPE and WKE start with the following initial wave-action spectra of Gaussian shape:

$$n^{\text{rad}}(k, 0) = g_0 \exp\left(\frac{-(k - k_s)^2}{\sigma^2}\right). \quad (34)$$

The values of parameters k_s and σ are chosen in such a way that the spectrum has enough space to spread to the left before building up strong condensate at the zero mode. On the other hand, k_s should not be too large that the direct cascade of energy [1,2] can evolve for a significantly long time before the right front of spectrum touches k_{cutoff} —the right boundary of the computational domain in the Fourier space. For these reasons, we set $g_0 = 1$, $k_s = 22$, $\sigma = 2.5$, and $k_{\text{cutoff}} = 43$ in the present work.

For WKE, we set $n_\omega(0) = n^{\text{rad}}(k, 0)/4\pi\omega$ with $\omega = k^2$. For GPE, we set $\hat{\psi}_{\mathbf{k}}(0) = |\hat{\psi}_{\mathbf{k}}(0)| \exp(i\phi_{\mathbf{k}}(0))$ with deterministic initial amplitudes $|\hat{\psi}_{\mathbf{k}}(0)| = \sqrt{\frac{n^{\text{rad}}(k, 0)}{4\pi k^2} \left(\frac{2\pi}{L}\right)^3}$ and random initial phases $\phi_{\mathbf{k}}(0)$ uniformly distributed in $[0, 2\pi)$ and statistically independent for each \mathbf{k} . Such an initial setting for GPE makes the RPA assumption satisfied at $t = 0$ and also corresponds to the initial PDF of intensities $J_{\mathbf{k}} = |\hat{\psi}_{\mathbf{k}}|^2$ being a δ -function.

A. GPE and WKE comparison for the short-time evolution

1. Spectrum evolution

Let us compare the spherically integrated wave-action spectra, $n^{\text{rad}}(k, t)$, from the GPE and the WKE simulations. The temporal evolution of $n^{\text{rad}}(k, t)$ is plotted in Fig. 1.

For the purposes of the present work, we define the nonlinear (kinetic) evolution timescale T_{kin} as the time it takes for the maximum of the spectrum to decrease to half of its initial value, which in this study is 15. First of all, we observe that the solutions of the GPE and the WKE agree well until $t = 25$. Of course, the results of the GPE obtained with 512^3 resolution show better agreement with the WKE than the results with 256^3 resolution. At small k 's, the inverse cascade of the GPE solution obtained with 256^3 resolution is initially slightly slower ($t < 10$) and then slightly faster ($t > 10$) than the inverse cascade of the WKE solution, whereas the spectra obtained from the GPE using 512^3 resolution keep closely behind those of the WKE. In the ultraviolet region—for large k 's—the solutions of the GPE with 256^3 and 512^3 resolutions start notably deviating from $t = 20$, and the former deviates also from the solutions of the WKE. This can be seen from the zoomed plot presented at the right top corner of Fig. 1. The

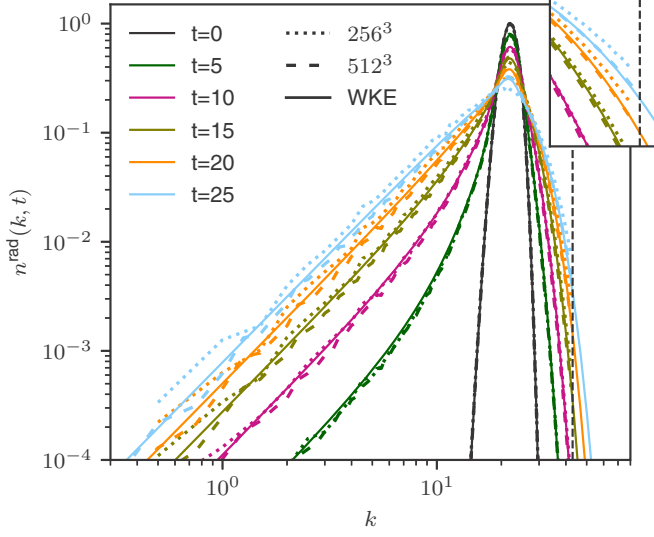


FIG. 1. Time evolution of $n^{\text{rad}}(k, t)$ for short time. Results for GPE with 256^3 and 512^3 resolutions and WKE at times $t = 0, 5, 10, 15, 20, 25$. The vertical dashed line marks the cutoff wave number for GPE numerics, $k_{\text{cutoff}} \approx 43$.

vertical dashed line in Fig. 1 indicates the cutoff wave number used in the numerical method of solving the GPE, $k_{\text{cutoff}} \approx 43$. The cutoff wave number of the WKE is twice as large as that of the GPE: $k_{\text{max}} = \sqrt{\omega_{\text{max}}} = 2k_{\text{cutoff}} \approx 86$.

Despite the remarkable agreement of the temporal evolution of the GPE and the WKE wave-action spectra, some minor differences appear at large scales (small k 's), probably due to the k -space discreteness. To give a more quantitative comparison between the solutions of the GPE and the WKE, we compute the wave-action and energy-based centroids K_N and K_E (the most particle- and energy-containing wave numbers, respectively) and their respective typical widths Δ_{K_N} and Δ_{K_E} in the interval $[0, k_{\text{cutoff}}]$ as follows:

$$\begin{aligned}
 K_N(t) &= \frac{1}{N_c(t)} \int_0^{k_{\text{cutoff}}} k n^{\text{rad}}(k, t) dk, \\
 \Delta_{K_N}(t) &= \sqrt{\frac{1}{N_c(t)} \int_0^{k_{\text{cutoff}}} (k - K_N)^2 n^{\text{rad}}(k, t) dk}, \\
 K_E(t) &= \frac{1}{H_c(t)} \int_0^{k_{\text{cutoff}}} k E^{\text{rad}}(k, t) dk, \\
 \Delta_{K_E}(t) &= \sqrt{\frac{1}{H_c(t)} \int_0^{k_{\text{cutoff}}} (k - K_E)^2 E^{\text{rad}}(k, t) dk}. \quad (35)
 \end{aligned}$$

In the above definitions, $E^{\text{rad}}(k, t) = k^2 n^{\text{rad}}(k, t)$ is the spherically integrated energy spectrum (full energy for the WKE and its linear-dynamics part for the GPE); $N_c(t) = \int_0^{k_{\text{cutoff}}} n^{\text{rad}}(k, t) dk$; and $H_c(t) = \int_0^{k_{\text{cutoff}}} E^{\text{rad}}(k, t) dk$. For the GPE, $N_c(t) = N$ is const, but $H_c(t) = H_2(t)$ varies around 1% at $t = 25$ (because GPE conserves the density of total energy H including the nonlinear-dynamics energy). For the WKE, $N_c(t)$ and $H_c(t)$ vary as well, since some waves cascade to modes with $k > k_{\text{cutoff}}$. Figure 2 shows the dynamics of the centroids and the typical widths for $t \in [0, 25]$. These

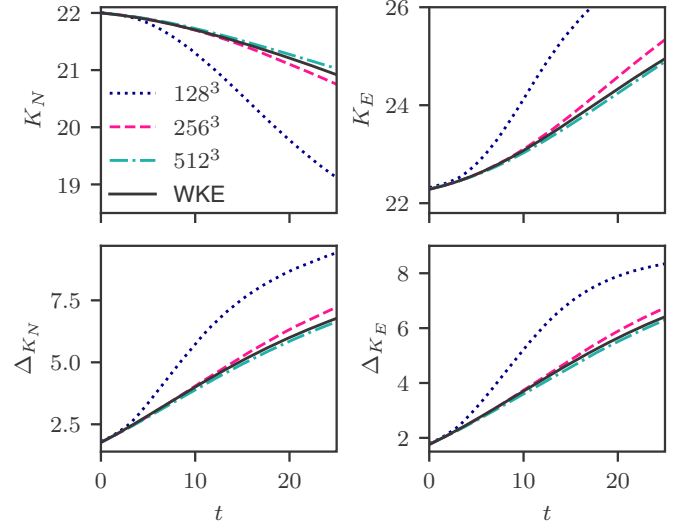


FIG. 2. Dynamics of the centroids of $n^{\text{rad}}(k, t)$ and $E^{\text{rad}}(k, t)$ and their respective typical widths Δ_{K_N} and Δ_{K_E} for short time, $t \in [0, 25]$. Results for the GPE with 128^3 , 256^3 , and 512^3 resolutions and for the WKE.

quantities are obtained by solving the WKE and the GPE with resolutions 128^3 , 256^3 , and 512^3 . At very short times, $t < 3$, the data obtained from the GPE simulations at all three resolutions and from the WKE demonstrate good agreement. The deviations between the solutions of the GPE with resolutions 256^3 and 512^3 remain rather small until much later times, $t \sim 25$. Since a good accuracy is obtained by solving the GPE with 512^3 resolution, in what follows all the GPE results are given with this resolution.

2. Verifying the WT assumptions for the GP settings

Here, the assumptions made in Sec. II for the four-wave weak WT will be discussed in the framework of the setup chosen for the GPE simulations. First of all, the condensate fraction C_0 is less than 5×10^{-7} until $t = 25$, and the wave number corresponding to the healing length is $k_\xi = 2.21$. This means that for almost all wave numbers ($k > k_\xi$), the influence of condensation is negligible and the nonlinearity remains small.

We compute the spatio-temporal spectral density of the wave function $\psi(\mathbf{r}, t)$ by performing Fourier transform of $\hat{\psi}(\mathbf{k}, t)$ with respect to the time variable over a finite window of size T_w . Thanks to the spatial isotropy of $\hat{\psi}(\mathbf{k}, t)$, we choose $k_x = k_y = 0$ and perform the Fourier transform in time for each k_z . The spatio-temporal spectral density is simply the surface of $|\hat{\psi}(k_x, \omega)|^2$.

Figure 3 displays the normalized spatio-temporal spectral density of $\psi(\mathbf{r}, t)$ over the time interval $t \in [12, 18]$, which is around T_{kin} . The normalization is performed along each line $k = \text{const}$ in the k - ω plane separately. It consists in a division of the spectral density function at the given fixed k by the value of its integral with respect to the variable ω taken over the interval $[0, \infty)$. The figure shows that the majority of the spectrum is concentrated close to the frequencies that satisfy the dispersion relation $\tilde{\omega}(k) = \omega(k) + 2N$ for the corresponding wave numbers; see (8). It should be noted that $\omega(k) = k^2$ is

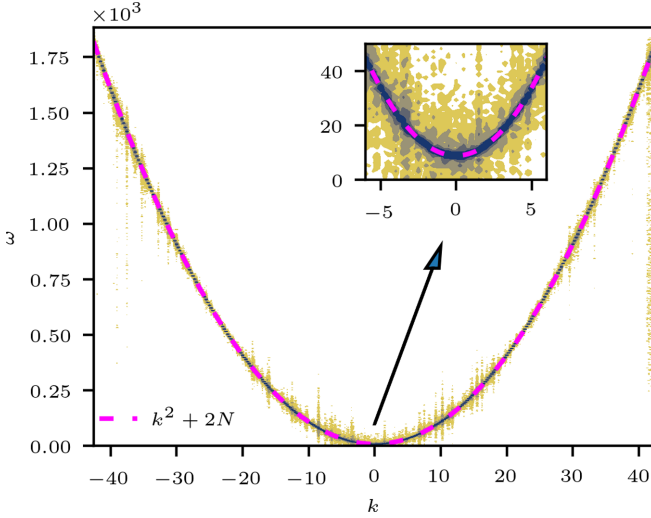


FIG. 3. Spatio-temporal spectral density of $\psi(\mathbf{r}, t)$ over the time interval $[12, 18]$.

the linear-wave dispersion relation, and $2N$ is the shift induced by the nonlinearity (this shift is shown in the small plot).

Moreover, because of the nonlinearity, a broadening of the frequency can be observed around $\tilde{\omega}(k)$: sufficiently narrow broadening implies the weak-wave regime. One can measure the nonlinear frequency broadening $\delta(k)$ directly from the spatial-temporal spectral density. Here, we define $\delta(k)$ for each fixed k in such a way that the integration of the spectral density over the interval of the width $\delta(k)$ centered at the ω -peak gives the value 0.99. To capture such information, the length of the time window T_w of FFT should be larger than both linear and nonlinear timescales, which are $\frac{2\pi}{\omega(k)}$ and $\frac{2\pi}{\delta(k)}$, respectively. Meanwhile, T_w should not be too large so that the spectrum does not vary much over T_w in order to provide good accuracy.

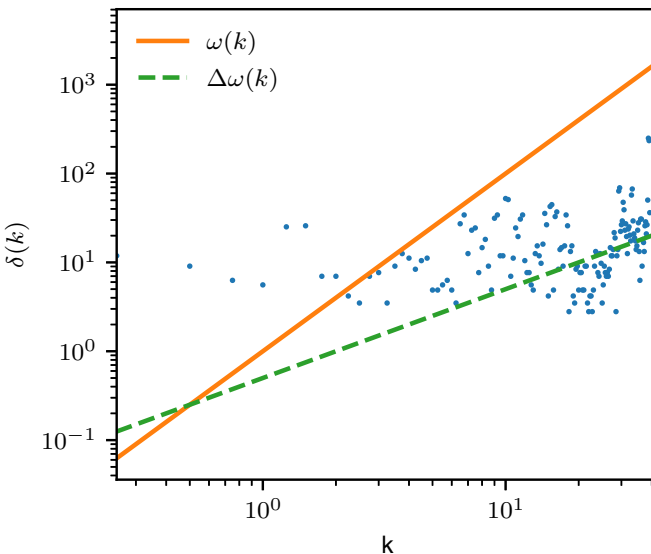


FIG. 4. Frequency broadening $\delta(k)$ (blue points) obtained from the spatial-temporal spectral density over the time interval $[12, 18]$.

Figure 4 presents the frequency broadening $\delta(k)$ obtained from Fig. 3. We choose the time window $t \in [12, 18]$ around $t = 15$, when the GPE gives good agreement with the WKE. The weak WT theory, on the one hand, requires the nonlinear timescales to be much greater than the linear ones [this amounts to the constraint $\delta(k) < \omega(k)$]. On the other hand, for solutions of the GPE in the discrete Fourier space to be in the continuous k -space regime assumed by the weak WT theory, $\delta(k)$ should be greater than the frequency distance between the adjacent wave modes, $\Delta\omega(k) = 2k\Delta k$. This condition is necessary to excite the nonlinear resonant and quasiresonant interactions among waves [1]. (For more discussion about the role of the quasiresonant interactions, see also [35–40].) One can see that there is a significant k -range for which most of the points (k, δ_k) lay in the domain bounded by $\omega(k)$ and $\Delta\omega(k)$.

It is interesting to see that $\delta(k)$ is greater than $\omega(k)$ at small k 's, which implies strong nonlinearity in the largest scales. However, Fig. 1 shows that the wave-action spectrum is small in this range. It reminds us that the “weak wave turbulence” assumption exactly means weakly nonlinear waves rather than weak waves: even if a particular mode is very weak, the linear term at its wave number can be overpowered by the nonlinear term because the former is proportional to the frequency (which is small at small k 's) and the latter is enhanced by contributions from the other modes in the system.

One can also observe in Fig. 4 that $\delta(k)$ sinks around $k = 22$ (where the initial waves have maximum amplitudes) and some of the points fall even below the $\Delta\omega(k)$ line. This is because the initial waves generate continuous cascades toward both low and large wave numbers. When $\delta(k)$ falls below the $\Delta\omega(k)$ line, the discreteness of the k -space becomes significant, and deviations from the weak WT theory should be expected.

Thus we can see in Fig. 4 that the range of wave numbers where the weak WT theory assumptions are satisfied at $t \sim 15$ is approximately $2 \lesssim k \lesssim 20$. This range becomes narrower for larger times.

B. GPE and WKE comparison for the long-time evolution

Having observed a very good quantitative agreement between the numerical solutions of the GPE and the WKE at the times up to about two kinetic times, we would now like to prolong the computations to longer times to see how such an agreement gradually degrades, and if a qualitative similarity survives at the late stages. In Fig. 5 centroids and related typical widths are plotted up to $t = 100$. The centroids of wave-action spectra start to deviate a little earlier than those of energy spectra. At late times, the former exhibits larger deviations. The typical widths Δ_{K_N} and Δ_{K_E} show even better correspondence—the curves obtained by the GPE and the WKE go very close until $t \approx 50$.

The comparison of the spectra obtained by solving the GPE and the WKE until $t = 100$ is given in Fig. 6. The disagreement between the GPE and the WKE takes place at both low values and high values of k starting around $t = 40$. Overall, the GPE is faster than the WKE for the direct cascade, but slower for the inverse cascade. This trend can also be observed in Fig. 5—the evolution of K_N of the GPE to small

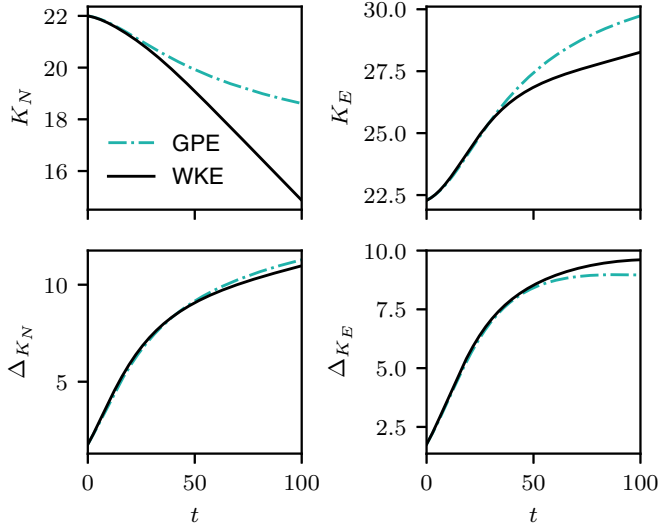


FIG. 5. Dynamics of the centroids of $n^{\text{rad}}(k, t)$ and $E^{\text{rad}}(k, t)$ and the corresponding typical widths. Results for the 512^3 GPE and the WKE for $t \in [0, 100]$.

k 's is slower than the evolution of K_N of the WKE, whereas the evolution of K_E to large k is faster.

The observed deviations between the long-term GPE and WKE spectra can be attributed to the following major factors: (i) failure of the conditions of the WKE applicability due to increased nonlinearity or/and increasing importance of the finite-box effects, and (ii) numerical effects due to differences of computational ranges and the discretization steps in the GPE and the WKE codes. Below, we will discuss these effects while trying to separate explicitly which one of them is the “failure of the weak WT theory” and which is “numerical.”

First of all, we note that the deviations are totally expected for the spectrum propagating into the region of small wave

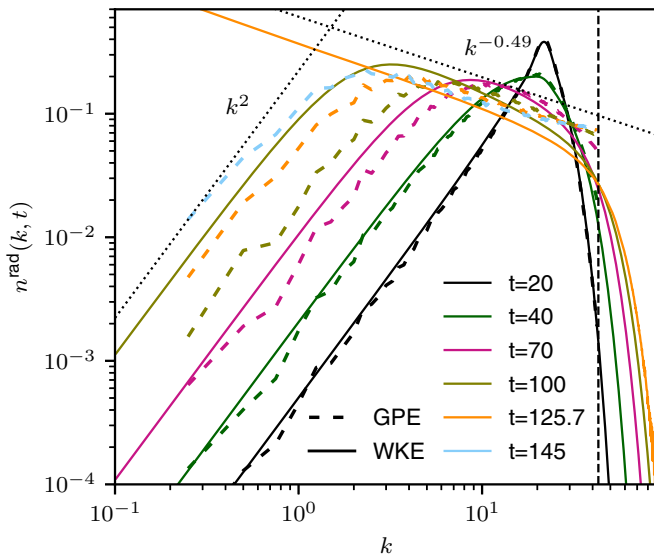


FIG. 6. Long-term evolution of $n^{\text{rad}}(k, t)$. Results for the 512^3 GPE and the WKE at $t = 20, 40, 70, 100, 125.7$, respectively, and for the GPE at 145.

numbers because of the failure of the weak WT theory in this range. Indeed, according to Fig. 4, even at $t \sim 15$ the nonlinear frequency broadening $\delta(k)$ is greater than the linear-wave frequency for $k \leq 2$, so the WKE description is not applicable there. Since the spectrum at low k is growing, this boundary of WKE applicability moves to higher k 's at later times.

An interesting and important fact is that, even though the GPE is slower than the WKE for small values of k , both the GPE and the WKE obey the global thermodynamic equilibrium scaling k^2 (the left black dotted line), but with different characteristic evolution times. Then considering the long-time evolution, it is important to keep in mind that the solution of the WKE is predicted to blow up at $k = 0$ at a finite time t^* [8–10,13], so that the WKE cannot be computed beyond this time without a modification of the model taking into account the zero-mode evolution. For the initial condition considered in the present paper, we found numerically that $t^* \approx 126.7$. Close to t^* , the evolution appears to be self-similar, with a transient power law forming in the inverse cascade $n^{\text{rad}}(k) \propto k^{-x^*}$ with exponent x^* which has a different value from the one in the inverse-cascade KZ solution, i.e., x^* differs from $1/3$. The most careful recent study of the self-similar formulation of the WKE [13] gives two values of x^* for the most accurate solutions, 0.44 and 0.48. Further, a similar behavior was observed in 512^3 simulations of the 3D GPE with a slightly different value, $x^* \approx 0.52$ [41]. In Fig. 6 we see that the late WKE spectra exhibit law $k^{-0.49}$ (indicated by a black dotted line), whereas the GPE scaling is slightly less steep, probably due to the spectrum pileup near k_{cutoff} .

Let us now concentrate on the differences that the GPE and the WKE exhibit for the inverse and the forward cascade ranges that may be attributed to the differences in the numerical setups for the GPE and WKE simulations. It is easy to see that for small wave numbers (e.g., $k < 10$), the curves obtained by the GPE show visible fluctuations starting from $t = 40$, while the results generated by the WKE keep good smoothness all the time. This behavior is to be expected considering the fact that the WKE deals with ensemble-averaged wave distributions and with a space of continuous wave number (allowing for using the grids in the k variable, which are finer at low k 's), whereas the GPE spectra are not ensemble- (or time-) averaged: the only averaging in this case is over spherical shells in the Fourier space, which contain fewer and fewer modes as one moves to smaller k 's.

Note that, even though the WKE grid can be refined close to $\omega = 0$, the WKE does not include the evolution of a condensate mode, unlike the GPE. Indeed, while the GPE solution evolves, the condensate fraction C_0 may start to grow. However, in the current simulations its final value is less than 5×10^{-5} at $t = 145$, so the influence of condensate in the GPE simulation can still be neglected. The fact that the WKE predicts condensation starting at $t^* \approx 126.7$ whereas no condensate growth is seen in the GPE simulation even at $t = 145$ could be qualitatively understood if we recall the condensation criterion for the weakly interacting 3D GPE: $E/N < k_{\text{max}}^2/3$ [42]. It turns out that for our initial condition, this criterion is well satisfied for the WKE but only marginally so for the GPE because the former has a cutoff wave number twice as big as that of the latter. In a separate simulation, we have verified that condensation does indeed occur for the GPE too if the

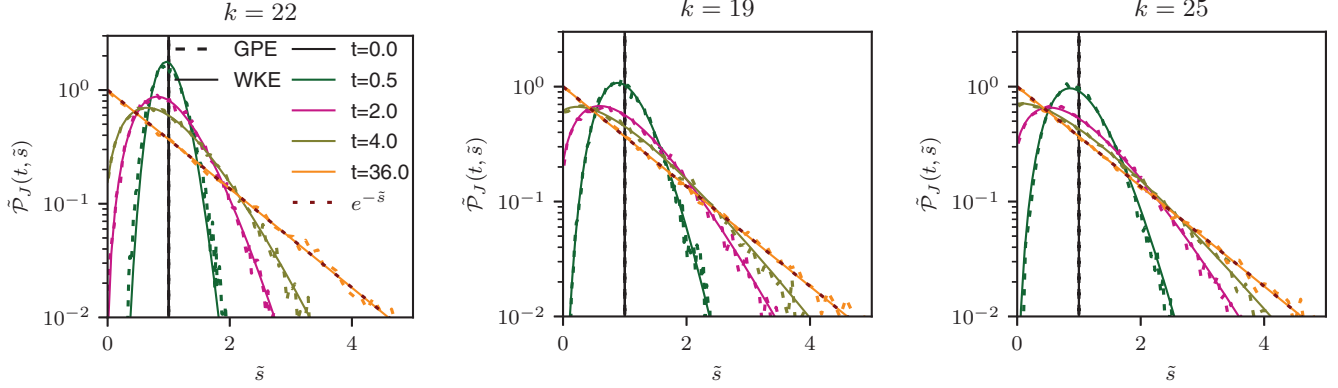


FIG. 7. Time evolution of the normalized probability density functions $\tilde{\mathcal{P}}_J(t, \bar{s})$. Results for 512^3 GPE and WKE for various k .

initial spectrum is shifted to smaller wave numbers (leading to smaller E/N).

On the other side, the high wave-number cutoff of the GPE results in the numerical effect of an accumulation of waves near k_{cutoff} , which affects the overall dynamics of the system. This is the well-known “bottleneck” phenomenon typical for many turbulent systems, which could roughly be described as the energy flux stagnation at scales slightly larger than the scales where the spectrum is depleted either by a dissipation (especially if the latter is of the hyperviscous type) or by a numerical cutoff (like in our case) [43–46]. It is difficult to break this restriction in numerical simulations since it is induced by the finite computational domain and finite space resolutions. However, the WKE can provide solutions for large values of k with an acceptable requirement of computational resources.

Finally, let us comment on the effect of discreteness of the wave-number space in the GPE simulations due to the finite size of the periodic box L —an effect that is not present in the WKE formulation, whose frequency space is continuous. Naively one could guess that this effect is most important in the low- k range. However, as seen in Fig. 4 for $t \sim 15$, the k -space discreteness becomes a problem at the high k 's and not the small ones. This is because at low k 's the nonlinear frequency broadening remains greater than the spectral distance between the adjacent linear eigenmodes (which is $2\pi/L = 1/4$ in the 512^3 runs). This picture persists for $t > 15$, and moreover the discrete effects become less important at high k 's too because of the bottleneck spectrum accumulation in this region, leading to an increase of the frequency broadening. To summarize, we believe that the finite-size effects are less important for understanding the deviations between the GPE and the WKE results compared to the other effects we have mentioned above.

C. Low- and high-order statistics

1. Comparison of the PDFs and the low-order cumulants (GPE and WKE)

Let us now consider the PDF of the transient states starting from the deterministic initial amplitudes and evolving towards an exponential PDF corresponding to a Gaussian wave-field statistics. We shall use here the previous setup (34) and analyze the evolution of the normalized PDF and the relative cumulants at the point $k = k_s = 22$ —the maximum point of

the initial spectrum, and the points $k = 19$ and 25 symmetrically placed around $k = 22$. Figures 7 and 8 display the temporal evolution of $\tilde{\mathcal{P}}_J(t, \bar{s})$ and $F^{(p)}(t)$, respectively. As expected, for all three modes the normalized PDFs for both the GPE and the WKE spectra evolve from the $\delta(\bar{s} - 1)$ at $t = 0$ to the final exponential distribution $e^{-\bar{s}}$. Overall, the results generated by the GPE agree well with the prediction derived from the WKE. Also, from Fig. 7 we see that the PDF at $k = 22$ evolves towards Gaussianity slower than the PDFs at $k = 19$ and 25 . This is consistent with our prediction that the rate of convergence to Gaussianity is faster for those k 's where the initial spectrum $n_k(0)$ has smaller values.

Figure 8 provides further validation of the statistical predictions derived from the WKE by plotting the relative cumulants of the first to fifth orders. All the cumulants finally tend to zero—the state corresponding to the Gaussian wave-field statistics (again, faster at $k = 19$ and 25 than at $k = 22$). For high orders, GPE cumulants start to deviate from those of the WKE after reaching a certain time. As explained above, the discreteness of the GPE modes does not allow the degree of averaging sufficient for generating an accurate PDF especially for large values of \bar{s} . The accuracy of high-order moments is also affected by such a discretization earlier in time than the accuracy of the low-order ones. As a consequence, in Fig. 8 for $t < 20$, the GPE gives a good picture of $F^{(p)}(t)$ up to the fifth order at $k = 22$, but at $k = 19$ and 25 good agreement with the WKE is preserved only up to $p = 4$.

2. High-order statistics using the WKE

Studying high-order statistics for a time-dependent problem requires us to produce ensemble realizations in order to collect the statistics. For the GPE simulations presented in this work, such a study is prohibiting. Instead, the weak WT theory provides a framework in which the high-order statistics can be studied.

To compute the PDF, we first obtain the numerical solution of the WKE, $n(t) = n_\omega(t)$. Then, we use the exact solution of evolution equation (20) for the PDF, i.e., formulas (24)–(26), where the deterministic initial data J have a Gaussian shape as a function of k , Eq. (34). For computing the higher-order cumulants $F^{(p)}(t)$, we use formula (30), where moments $M^{(p)}$ are the integrals of functions $\bar{s}^p \tilde{\mathcal{P}}_J(\bar{s}, t)$. Thus, knowing the numerical solution of the WKE in the framework of weak WT

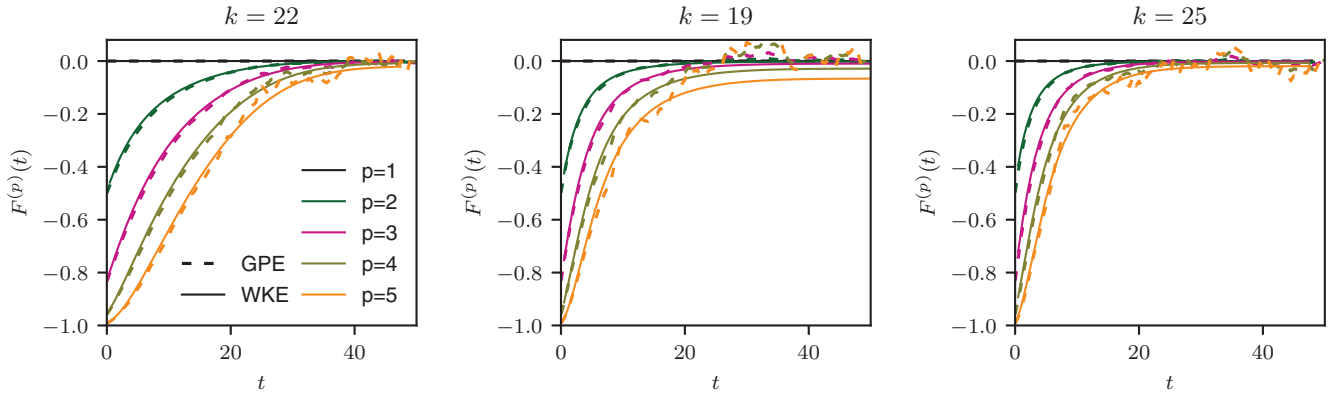


FIG. 8. Time evolution of the relative cumulants $F^{(p)}(t)$. Results for 512^3 GPE and WKE for various k .

theory, one can restore the high-order statistics using exact formulas.

The goal of this section is to represent the transition between deterministic initial data with a Gaussian k -distribution as a motion of fronts with respect to \tilde{s} and p variables. Ahead of the fronts, PDFs and cumulants deviate significantly from the Gaussian statistics, whereas behind the fronts they are very close to the Gaussian statistics.

To define such fronts, we set a threshold value of the relative deviation of the statistics from Gaussian equal to 1% since this value becomes noticeable on the plots. Then, for each time moment t we find the points \tilde{s} and p , for which the relative PDF $\tilde{\mathcal{P}}(t, \tilde{s})/\mathcal{P}_G(\tilde{s})$ and cumulant $F^{(p)}(t)$ deviate from corresponding curves of Gaussian statistics by 1%. In what follows, for these points we use notations $\tilde{s}^*(t)$ and $p^*(t)$, respectively.

Figure 9(a) shows the relative PDFs computed at $k = 22$. The black dot denotes the point $\tilde{s} = \tilde{s}^*(t)$ where the curve corresponding to $t = 50$ deviates from the limiting dashed line by 1%, i.e., where the ratio of the PDF and the exponential PDF $\mathcal{P}_G(\tilde{s})$ takes the value 0.99. The dynamics of the point $\tilde{s}^*(t)$ illustrates a front moving towards large \tilde{s} as $t \rightarrow \infty$. Behind this front, the PDF asymptotically approaches the exponential one, whereas ahead of this point it still deviates by more than 1%. Figure 9(b) displays the dynamics of $\tilde{s}^*(t)$ for different values of k , showing its acceleration in the final phase, which depends on the wave number.

Let us now consider the behavior of the high-order relative cumulants. In Fig. 10(a) the cumulants as functions of the order p are shown at different times for $k = 22$. Similarly, the point $p^*(t)$ corresponds to the value of p for which at the time moment t the cumulant $F_k^{(p)}$ takes the value -0.01 . Figure 10(b) shows the propagation of the front associated with the motion of the point $p^*(t)$.

We should mention here an obvious similarity between the evolution of relative PDFs as functions of \tilde{s} and of the cumulants as functions of p , when t is large enough.

V. DISCUSSION AND CONCLUSIONS

The main goal of the present paper is to test the weak wave turbulence theory by comparing numerical simulations of the Gross-Pitaevskii equation (GPE) and the wave-kinetic

equation (WKE). Several fundamental constraints have to be kept in mind during such a comparison.

First, the weak WT theory assumes that the wave must be weak enough, but not too weak. Namely, the waves have to be weak so that the linear dynamics is faster than the nonlinear transfers of energy between the wave modes, but also strong enough so that the nonlinear frequency broadening is larger than the frequency spacing between the nearby modes in the wave-number space, so that the continuous k -space limit can be considered. We have checked these conditions in our numerical simulations. Figure 4 shows that the range of wave numbers, where these two weak WT theory assumptions

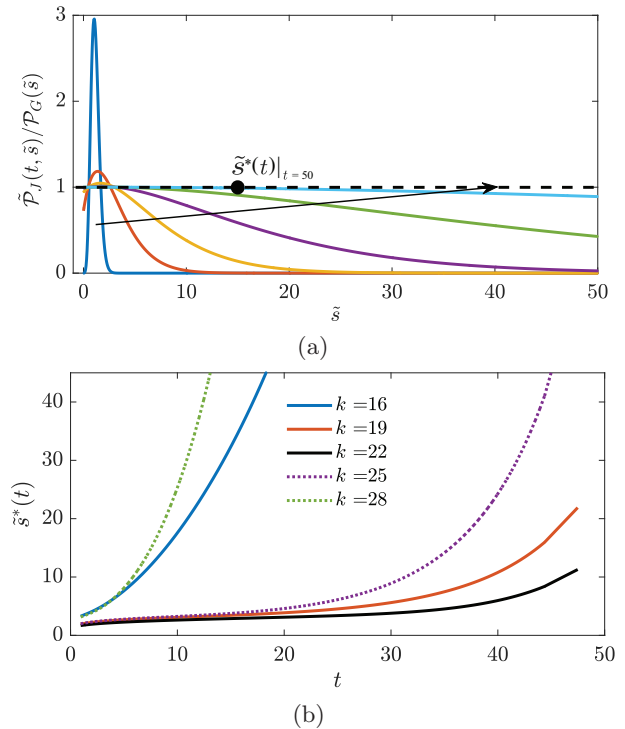


FIG. 9. (a) Relative probability density functions computed using the numerical solutions of WKE for different time moments and $k = 22$. The arrows show time evolution and pass from the left to the right through the curves corresponding to $t = 1, 10.8, 20.6, 30.4, 40.1, \text{ and } 50$. The horizontal dashed line shows the Gaussian distribution. (b) Motion of the front $\tilde{s}^*(t)$ for different values of k .

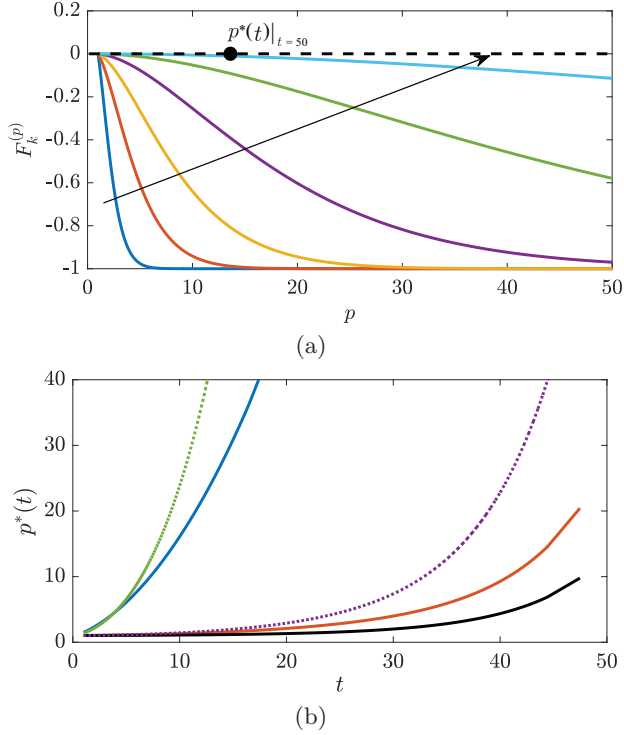


FIG. 10. (a) Cumulants as a function of their order p [same times as in Fig. 9(a)]. (b) Motion of the front $p^*(t)$ for different values of k [as in Fig. 9(b)]. The bottom black line corresponds to $k = k_s$.

are satisfied simultaneously at $t \sim 15$, is $2 \lesssim k \lesssim 20$, and we found that this range becomes narrower for larger times. It is then rather remarkable that we found a nearly perfect agreement between the WKE and the GPE results up to $t \sim 30$, which is about two nonlinear (kinetic) evolution times. To characterize our comparisons, we have looked directly at the spectra, as well as at their global characteristics—the energy and the particle centroids and typical widths. Another surprising fact is that even the relatively low 256^3 resolution of GPE simulations leads to a reasonably accurate agreement between the WKE and the GPE results, even though, naturally, the accuracy is better for 512^3 (and not at all good for 128^3).

We have also looked numerically at the probability density functions (PDFs) of the wave intensities, both using GPE simulations (directly) and the weak WT theory (using the analytical solution for the PDF obtained in [21]). Here as well, we have seen an excellent agreement for the early evolution up to $t \sim 30$ and, qualitatively, far beyond this time. In fact, in agreement with the theoretical predictions, the PDFs of the wave intensities tend to exponentially decreasing functions corresponding to Gaussian wave fields. At $t \sim 30$, the PDFs have practically attained the final exponential shape, and the only difference between the weak WT theory and the GPE results is that the PDFs obtained for the GPE have noisy tails due to insufficient averaging. It is important to emphasize that, in agreement with the theoretical predictions [1,17,21], the evolution toward Gaussianity occurs at the kinetic timescale (in our case $t \sim 15$), i.e., at the same characteristic time as that for the spectrum evolution, rather than a much shorter timescale. On the other hand, the evolution of the wave intensity PDF from deterministic to exponential in simulations

of the 2D GPE was previously observed in [47], where it was reported that the PDF evolution time is much faster than that for the spectrum, which at first glance seems at odds with our findings. This “contradiction” seems to originate from the difference in the definition of the characteristic evolution time for the spectrum: in the present paper, we define it as a time needed for the spectrum to experience order-1 changes (specifically, for its maximum to become twice as small), whereas a much longer time needed for the spectrum to approach thermodynamic equilibrium is discussed in [47]. With this remark in mind, we see that our results do not contradict those of [47]: the PDF core evolves to the exponential shape at the kinetic timescale (even though the PDF tails and the cumulants evolve slower; see Figs. 8–10) whereas the spectrum, while evolving initially at the kinetic timescale (by definition), keeps evolving for much longer up to the blowup time. Note also that the statement about the PDF evolution time has to be adjusted in the case of sharply peaked PDFs. From (20), for the PDF core ($s \sim n$) we have the following estimate for the characteristic PDF evolution time: $T_{\text{PDF}} \sim T_{\text{kin}}(n/\delta s)^2$, where δs is the width of the PDF peak. In particular, our δ -shaped initial PDF means that formally the initial PDF evolution time is zero. We would also like to mention a previous study of a model 2D three-wave system [20] where a comparison was made for the PDF and cumulants obtained from a DNS and the numerics of the weak WT closure equations for these statistical objects up to $t \sim 0.3T_{\text{kin}}$ (no analytical solution for the PDF was available at that time yet). They arrived at favorable conclusions for the validity of the weak WT theory for the considered three-wave system.

Secondly, weak WT theory assumes a “propagation of chaos” property: the random phase and amplitude (RPA) statistics of the initial data should survive through the nonlinear (kinetic) evolution time [1,15,16]. Naively, one could think that the RPA statistics could be tested numerically by directly accessing the joint statistics of the Fourier modes. However, it is clear that the RPA cannot propagate in its pure form for the entire set of wave modes. Instead, it should survive only in the sense of distributions, e.g., the statistical moments and the reduced PDFs restricted to a smaller number of waves [1,17]. Numerical studies of these issues would be a good subject for future research. In the present work, however, we see indirect evidence for the propagation of chaos in the fact that the WKE provides a good description of the wave spectrum for at least two nonlinear kinetic times.

It is interesting that a qualitative agreement of the GPE and WKE results is also observed for the long-time evolution, up to $t \sim 100$ and even beyond (but obviously for $t < t^*$, where t^* is the finite-time moment when the solution of the WKE blows up at zero mode). In particular, in both simulations a self-similar inverse cascade with two power-law scalings (with exponents ~ 2 and ~ -0.49) is observed for t close to t^* . However, significant differences arise at the lowest and the highest scales for $t \gtrsim 40$. In addition to the shrinking of the weak WT theory applicability range, which we mentioned before, the factors causing the deviations include the differences in the minimal and the maximal scales used for the WKE and GPE. Generally, one can afford a much greater range of wave numbers in the WKE than in the GPE. In our WKE simulations, we had the minimal wave number at about 0.1

and the maximal wave number at 86, whereas in 512³ GPE these boundaries were at 0.25 and 43, respectively. Having a lower maximum wave number leads to a visible accumulation of the spectrum in the highest wave numbers, whereas in the WKE results the forward cascade spreads freely to much higher k 's. It is then surprising that the energy centroid for the WKE appears to move to the right more slowly than the one for the GPE. It is equally surprising to see the inverse cascade moving toward low k 's faster for the WKE than for the GPE. Indeed, this result is at odds with a common view that the nonlinearity becomes stronger during the inverse cascade process, so the GPE system should switch from the kinetic to a dynamic timescale, which is shorter. At present, we do not have an explanation for this behavior.

Once again, we would like to reiterate our view that the late-time deviations between the GPE and the WKE evolution are due to a combination of two equally important factors: breakdown of WKE validity conditions, and the existence of the high-frequency cutoffs, which were different for the GPE and the WKE simulations.

The present work was restricted to the situations when the condensation fraction remains negligible. A direct consequence of the condensation is that the system goes into a three-wave regime—namely the acoustic wave turbulence. The corresponding WKE for waves on the background of a strong background condensate was derived in [3]. Numerical simulations of the GPE were previously performed for such a regime in [4,5,48], which were aimed at comparing their results to the stationary KZ solution of the respective three-wave WKE. However, in future it would be interesting to study evolving WT in this regime and confront the GPE and the WKE results in a way similar to how it was done in the present paper, aimed at testing the validity of the WT approach in the presence of a strong condensate component.

ACKNOWLEDGMENTS

This work is funded by the Simons Foundation Collaboration grant Wave Turbulence (Award ID 651471). Part of this work was granted access to the high-performance computing facilities under GENCI (Grand Equipement National de Calcul Intensif) A0102A12494 (IDRIS and CINES), the OPAL infrastructure from Université Côte d'Azur, supported by the French government, through the UCAJEDI Investments in the Future project managed by the National Research Agency (ANR) under Reference No. ANR-15-IDEX-01, and the SIGAMM infrastructure [49] hosted by Observatoire de la Côte d'Azur and supported by the Provence-Alpes Côte d'Azur region.

APPENDIX A: DERIVATION OF THE ANGLE-AVERAGED KINETIC EQUATION

When the wave fields are statistically isotropic, the averaging of WKE (9) can be done by integrating it over the unit sphere S_1 and performing the internal angle integrations. This will change the variables \mathbf{k} and \mathbf{k}_j , $j = 1, 2, 3$, of (9) to variables $k = |\mathbf{k}|$ and $k_j = |\mathbf{k}_j|$, respectively. In what follows, we also use the representations $d\mathbf{k} = k^2 dk d\Omega$ and $d\mathbf{k}_j = k_j^2 dk_j d\Omega_j$, where $d\Omega$ and $d\Omega_j$ are the area elements

on the unit spheres associated with the vectors \mathbf{k} and \mathbf{k}_j , respectively. Isotropy of the spectrum means that it depends only on the modulus of the vector \mathbf{k} , i.e., $n_{\mathbf{k}} = n_k$.

Denoting $n_j = n_{\mathbf{k}_j}$, $\omega = \omega_{\mathbf{k}}$, and $\omega_j = \omega_{\mathbf{k}_j}$, one can write the averaged WKE as follows:

$$\begin{aligned} \frac{dn_k}{dt} &= \frac{1}{4\pi} \int_{S_1} \frac{dn_{\mathbf{k}}}{dt} d\Omega \\ &= \int \mathcal{P} \delta_{1\omega}^{23} n_k n_1 n_2 n_3 \left(\frac{1}{n_k} + \frac{1}{n_1} - \frac{1}{n_2} - \frac{1}{n_3} \right) d123, \end{aligned} \quad (\text{A1})$$

where

$$\begin{aligned} \delta_{1\omega}^{23} &= \delta(\omega + \omega_1 - \omega_2 - \omega_3), \quad d123 = k_1^2 k_2^2 k_3^2 dk_1 dk_2 dk_3, \\ \mathcal{P} &= \int \delta_{1\mathbf{k}}^{23} d\Omega d\Omega_1 d\Omega_2 d\Omega_3, \end{aligned} \quad (\text{A2})$$

where $\delta_{1\mathbf{k}}^{23} = \delta(\mathbf{k} + \mathbf{k}_1 - \mathbf{k}_2 - \mathbf{k}_3)$. To compute \mathcal{P} , we first recall that the Dirac δ -function can be represented as the Fourier transform of unity:

$$\delta_{1\mathbf{k}}^{23} = \frac{1}{(2\pi)^3} \int_{\mathbb{R}^3} \exp[-i\mathbf{r} \cdot (\mathbf{k} + \mathbf{k}_1 - \mathbf{k}_2 - \mathbf{k}_3)] d\mathbf{r}. \quad (\text{A3})$$

Therefore, substituting (A3) into (A2) and changing the order of integration, one obtains

$$\mathcal{P} = \frac{1}{(2\pi)^3} \int_{\mathbb{R}^3} P(\mathbf{r}) d\mathbf{r}, \quad (\text{A4})$$

where

$$P(\mathbf{r}) = \int \exp[-i\mathbf{r} \cdot (\mathbf{k} + \mathbf{k}_1 - \mathbf{k}_2 - \mathbf{k}_3)] d\Omega d\Omega_1 d\Omega_2 d\Omega_3. \quad (\text{A5})$$

Let us pass to the angular coordinates of spherical surfaces, (φ, θ) , where $0 \leq \varphi \leq 2\pi$, $0 \leq \theta \leq \pi$ (and the same for φ_j, θ_j):

$$d\Omega = \sin\theta d\theta d\varphi, \quad d\Omega_j = \sin\theta_j d\theta_j d\varphi_j, \quad j = 1, 2, 3.$$

Defining θ_j to be the angles between the vectors \mathbf{k}_j and \mathbf{r} , we have

$$\mathbf{r} \cdot \mathbf{k}_j = rk_j \cos\theta_j, \quad j = 1, 2, 3,$$

where $r = |\mathbf{r}|$. Similarly,

$$\mathbf{r} \cdot \mathbf{k} = rk \cos\theta.$$

Thus, one can write

$$\begin{aligned} \int e^{-i\mathbf{r} \cdot \mathbf{k}} d\Omega &= \int_0^{2\pi} d\varphi \int_{-1}^1 d\chi e^{-irk\chi} \\ &= -\frac{2\pi}{irk} \exp(-irk\chi) \Big|_{\chi=-1}^1 = \frac{4\pi}{rk} \sin(rk), \end{aligned} \quad (\text{A6})$$

where $\chi = \cos\theta$.

Using (A6) and the similar results for the integrals of $e^{-i\mathbf{r} \cdot \mathbf{k}_j}$, $j = 1, 2, 3$, one can write for the integral in (A5)

$$P(\mathbf{r}) = \frac{(4\pi)^4}{r^4} \frac{\sin(rk)}{k} \prod_{i=1}^3 \frac{\sin(rk_i)}{k_i}.$$

Substituting this into (A4) using the representation $d\mathbf{r} = r^2 dr d\Omega_{\mathbf{r}}$, and using *Mathematica* for integration, we get the

following expression:

$$\begin{aligned} \mathcal{P} &= \frac{32\pi}{kk_1k_2k_3} \int d\Omega_{\mathbf{r}} \int_0^\infty \frac{\sin(rk)}{r^2} \prod_{j=1}^3 \sin(rk_j) dr \\ &= \frac{8\pi^3}{kk_1k_2k_3} (-|k+k_1-k_2-k_3| - |k-k_1+k_2-k_3| \\ &\quad + |k+k_1+k_2-k_3| - |k-k_1-k_2+k_3| \\ &\quad + |k+k_1-k_2+k_3| + |k-k_1+k_2+k_3| \\ &\quad + |-k+k_1+k_2+k_3| - |k+k_1+k_2+k_3|). \end{aligned}$$

This expression can be considerably simplified after taking into account the four-wave frequency resonance condition

$$k^2 + k_1^2 = k_2^2 + k_3^2.$$

This leads to

$$\mathcal{P} = \frac{32\pi^3}{kk_1k_2k_3} \min(k, k_1, k_2, k_3).$$

Substituting this into (A1), we obtain the angle-averaged WKE:

$$\frac{dn_k}{dt} = \frac{32\pi^3}{k} \int \min(k, k_1, k_2, k_3) \delta_{1\omega}^{23} n_k n_1 n_2 n_3 \left(\frac{1}{n_k} + \frac{1}{n_1} - \frac{1}{n_2} - \frac{1}{n_3} \right) k_1 k_2 k_3 dk_1 dk_2 dk_3. \quad (A7)$$

The last point, which we shall address here, is passage in (A7) to the frequency variables $\omega = k^2$ and $\omega_j = k_j^2$, $j = 1, 2, 3$. Using the expressions $k = \sqrt{\omega}$, $dk = \frac{1}{2}\omega^{-1/2}$, $k_j = \sqrt{\omega_j}$, $dk_j = \frac{1}{2}\omega_j^{-1/2}$, and denoting $n_\omega = n_k$ and

$$S(\omega, \omega_1, \omega_2, \omega_3) = \min(\sqrt{\omega}, \sqrt{\omega_1}, \sqrt{\omega_2}, \sqrt{\omega_3}),$$

one obtains (10) from (A7).

APPENDIX B: EXTRA NUMERICAL DETAILS FOR THE WKE

An important block of the algorithm for solving the WKE, which should be mentioned first, is an accurate and fast computation of the collision integral on the RHS of (12). To perform such a computation, the cubature formulas proposed in [13] are applied, which requires us to decompose the domain of integration Δ_ω in (13) and (14). In our study, Δ_ω is represented as $\Omega_1 \cup \Omega_2$ (gray area in Fig. 11), where

$$\Omega_1 = \{(\omega_2, \omega_3) : \omega_2, \omega_3 \geq 0, 0 \leq \omega_2 + \omega_3 - \omega \leq \omega_{\max}\},$$

$$\Omega_2 = \{(\omega_2, \omega_3) : \omega_2, \omega_3 \leq \omega_{\max}, \omega_2 + \omega_3 - \omega \geq \omega_{\max}\}.$$

The integrands of the RHSs of (13) and (14) have singularities along the lines $\omega_2 = \omega$, $\omega_3 = \omega$, $\omega_2 = \omega_{\min}$, $\omega_3 =$

ω_{\min} , $\omega_2 + \omega_3 - \omega = \omega_{\min}$ denoted by dashed lines in Fig. 11, where the first- and higher-order derivatives of the integrands can have discontinuities. Therefore, to design cubature formulas with an exponential rate of convergence, Δ_ω must be cut along these lines and decomposed into a triangular, a rectangular, and a trapezoidal subdomain, as shown in Fig. 11. Inside each subdomain, the integrands are infinitely differentiable functions; see [13] and the reasoning presented there. Each of the subdomains is mapped onto the reference square $[-1, 1]^2$ (see [50] for additional details), and tensor products of the modified Clenshaw-Curtis formulas are used to compute the integrals. It should be noted that, in contrast to the formulation considered in [13], here we have a bounded domain of integration (gray area in Fig. 11), which somewhat simplifies the problem. The contributions to the collision term from the triangles Δ_1, Δ_2 are the integrals of the terms $S_\omega^{23} n_c n_3$ and $S_\omega^{23} n_c n_2$ in (14), respectively. The contribution from the domain Ω_2 is the integral of $S_\omega^{23} n_2 n_3$. Integration over other subdomains of Δ_ω includes all the terms in (13) and (14).

Now, let us address the problem of approximating the solution of the WKE, $n_\omega(t)$. Here, first of all one should choose an appropriate interval of approximation with respect to the variable ω . Since the spectrum vanishes at large ω very rapidly, it is enough to build approximation on the finite interval $[\omega_{\min}, \omega_{\max}]$ with large enough ω_{\max} and set $n_\omega(t) = 0$ for any $t < T$ and $\omega > \omega_{\max}$. One should also take into account that the solution of the WKE blows up at the zero mode at some finite time t^* . Moreover, in the vicinity of $t = t^*$ the spectrum demonstrates a self-similar behavior with constant value at small ω ; see [8–10,13] for details. To exclude the singularity at $\omega = 0$, we choose a small positive ω_{\min} and fix the value $n_\omega(t) = n_{\omega_{\min}}(t)$ for all $\omega < \omega_{\min}$ at a given time moment $t < T$. This value is included in the integral over the thin layer between the dashed line and the outer boundary of Δ_ω (see Fig. 11). Here, following the above results, we set $T = 100$.

For approximating WKE with respect to the time variable, we use the Runge-Kutta method of order 2 (RK2), we introduce the uniform grid with the step dt and the nodes $t_j = jdt$, $j = 0, 1, \dots$, and we implement an explicit time-marching

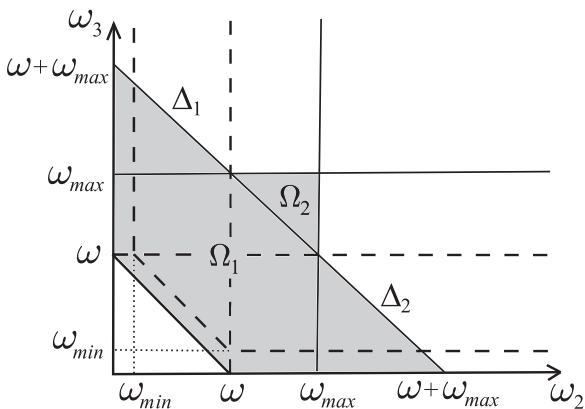


FIG. 11. Domain of integration Δ_ω in the plain (ω_2, ω_3) and its decomposition.

TABLE I. Convergence of the algorithm for solving the WKE for the fixed $M = 128$, $t = 100$, and various values of the time step dt .

dt	$R_{dt}(n)$	$R_{dt}(K_N)$	$R_{dt}(\Delta_{K_N})$	$R_{dt}(K_E)$	$R_{dt}(\Delta_{K_E})$
2	6.75×10^{-3}	1.98×10^{-3}	1.03×10^{-3}	6.43×10^{-5}	9.51×10^{-5}
1	1.72×10^{-3}	4.99×10^{-4}	2.58×10^{-4}	1.58×10^{-5}	2.33×10^{-5}
1/2	4.32×10^{-4}	1.25×10^{-4}	6.45×10^{-5}	3.89×10^{-6}	5.75×10^{-6}
1/4	1.08×10^{-4}	3.12×10^{-5}	1.61×10^{-5}	9.65×10^{-7}	1.43×10^{-6}
1/8	2.71×10^{-5}	7.80×10^{-6}	4.02×10^{-6}	2.40×10^{-7}	3.55×10^{-7}

scheme. Then, we denote $n^{[j]} = n^{[j]}(\omega) = n_\omega(t_j)$ and approximate the function $n^{[j]}(\omega)$ on the segment $[\omega_{\min}, \omega_{\max}]$ by the interpolation polynomial with Chebyshev nodes. For this we use the barycentric interpolation formula from [51],

$$p_M[n^{[j]}](\omega) = \sum_{m=1}^M \frac{\xi_m n^{[j]}(\omega_m)}{\mathcal{L}(\omega) - y_m} \bigg/ \sum_{m=1}^M \frac{\xi_m}{\mathcal{L}(\omega) - y_m}, \quad (\text{B1})$$

where $\xi_m = \frac{1}{T_M'(y_m)} = (-1)^{m-1} \sin(\frac{2m-1}{2M}\pi)$ are the weights of interpolation; $T_M(y)$ is the Chebyshev polynomial of the degree M ; y_m are zeros of $T_M(y)$, $m = 1, \dots, M$; $\mathcal{L}(\omega)$ is the linear mapping of the segment $[\omega_{\min}, \omega_{\max}]$ to $[-1, 1]$; and $\omega_m = \mathcal{L}^{-1}(y_m)$ are the interpolation nodes.

We also use the rational variant of (B1), which turns out to be a very efficient way of adapting the approximation to singularities of the solution; see [52,53]. In our case, the singularities are related with a huge length of the considered ω -interval (up to seven decades) and with the blow-up of the solution at the zero mode. To obtain the rational barycentric interpolation, we fix the weights ξ_m of (B1), but instead of the Chebyshev nodes y_m we use the transformed ones $\tilde{y}_m = g(y_m)$, $m = \overline{1, M}$. Here, the mapping $g: [-1, 1] \rightarrow [-1, 1]$ is a bijection, which has an analytical continuation to the complex plain. This continuation must be reversible, and the inverse mapping g^{-1} must take the singular point $\tilde{y}_1^* = \mathcal{L}(0)$ far enough from the segment $[-1, 1]$. Several possibilities of defining $g(y)$ are discussed in [53–55]. However, the straightforward application of these formulas leads to a very strong concentration of the nodes in the vicinity of $\omega = 0$ and bad resolution of the initial Gaussian peak centered at $\omega = k_s^2$.

To take into account both singular points $\tilde{y}_1^* = \mathcal{L}(0)$ and $\tilde{y}_2^* = \mathcal{L}(k_s^2)$, we used the idea from [56], which allows one to write the mapping in the form

$$g = \left(\frac{g_1^{-1} + g_2^{-1}}{2} \right)^{-1},$$

where the superscript “ -1 ” means the inversion of a function; g_1^{-1} , g_2^{-1} serve for mapping the singular points \tilde{y}_1^* and \tilde{y}_2^* ,

respectively. In our case,

$$g_i^{-1}(\tilde{y}) = \frac{a^+ - a^- + 2 \sinh^{-1} \frac{\tilde{y} - \tilde{y}_i^*}{\epsilon_i}}{a^+ + a^-},$$

$$a^\pm = \sinh^{-1} \frac{1 \pm \tilde{y}_i^*}{\epsilon_i},$$

where $i = 1, 2$, and ϵ_1, ϵ_2 are the small positive parameters used for tuning the densities of concentration of nodes in the vicinities of \tilde{y}_1^* and \tilde{y}_2^* , respectively. The closer $\epsilon_{1,2}$ are to zero, the higher is the density of the concentration. Basically, we set $\epsilon_1 = 10^{-4}$, $\epsilon_2 = 10^{-1}$. It is worth noting that these parameters also have an important mathematical meaning. For the details about this issue, we refer the reader to [53,54]. The described mapping g in combination with the barycentric representation (B1) allows one to achieve high accuracy even using coarse grids. However, it also requires some modifications of the formulas for integrating the obtained spectra.

To compute the centroids by formulas (35), we first make the change of the variable $k = \sqrt{\omega}$, then we use the mapping $\omega = \mathcal{L}^{-1} \circ g(y)$ with the Jacobian

$$J_{\mathcal{L}g}(y) = \frac{\omega_{\max} - \omega_{\min}}{1/[g_1' \circ g_1^{-1} \circ g(y)] + 1/[g_2' \circ g_2^{-1} \circ g(y)]},$$

and, finally, for integration with respect to the variable $y = g^{-1} \circ \mathcal{L}(\omega)$, we use the Clenshaw-Curtis formulas; see [57].

In numerical tests, we checked the convergence of the proposed method by observing the quantity

$$R_M(n) = R_{M,t}(n) = \frac{\max_{\omega} |n_M(\omega, t) - n_{2M}(\omega, t)|}{\max_{\omega} |n_{2M}(\omega, t)|}$$

obtained in computations with the fixed and small enough value of the time step dt , where $n_M(\omega, t) = p_M[n^{[j]}](\omega)$ is the rational interpolation of the spectrum with M nodes; see (B1). Here, it is assumed that for computing the collision integral, we use the cubature formulas with M^2 nodes in each subdomain of Ω . We also computed the quantities

$$R_M(\mathfrak{x}) = R_{M,t}(\mathfrak{x}) = \frac{|\mathfrak{x}_M(t) - \mathfrak{x}_{2M}(t)|}{\mathfrak{x}_{2M}(t)},$$

TABLE II. Convergence of the algorithm for solving the WKE for the fixed $dt = 0.25$, $t = 50$, and various values of the number M of the nodes of spatial grids.

M	$R_M(n)$	$R_M(K_N)$	$R_M(\Delta_{K_N})$	$R_M(K_E)$	$R_M(\Delta_{K_E})$
32	3.61×10^{-3}	8.98×10^{-4}	8.37×10^{-4}	7.87×10^{-4}	3.73×10^{-3}
64	1.54×10^{-5}	4.37×10^{-6}	1.45×10^{-6}	7.98×10^{-7}	1.01×10^{-5}
128	1.85×10^{-10}	6.70×10^{-9}	1.50×10^{-9}	7.49×10^{-11}	4.94×10^{-10}

TABLE III. Values of $R_{dt}(n)$ obtained with the fixed $M = 256$ at $t \approx 125.74$.

dt	0.16	0.08	0.04	0.02	0.01	0.005
$R_{dt}(n)$	0.0031	8.7×10^{-4}	1.9×10^{-4}	4.9×10^{-5}	1.2×10^{-5}	3.1×10^{-6}

where \mathfrak{x} denotes one of the functions $K_N(t)$, $K_E(t)$, $\Delta_{K_N}(t)$, $\Delta_{K_E}(t)$ determined in (35), and the subscript M stands for the number of nodes of a spatial grid used for the approximation of the solution and for the number of nodes of all the applied formulas for numerical integration.

By analogy, we computed the values

$$R_{dt}(n) = R_{dt,t}(n) = \frac{\max_{\omega} |n_{dt}(\omega, t) - n_{dt/2}(\omega, t)|}{\max_{\omega} |n_{dt/2}(\omega, t)|}$$

with the fixed and large enough number of space nodes, where $n_{dt}(\omega, t)$ is the solution obtained using RK2 with the time step dt . In addition, we computed the values

$$R_{dt}(\mathfrak{x}) = R_{dt,t}(\mathfrak{x}) = \frac{|\mathfrak{x}_{dt}(t) - \mathfrak{x}_{dt/2}(t)|}{|\mathfrak{x}_{dt/2}(t)|},$$

where $\mathfrak{x}_{dt}(t)$ is determined similarly to $n_{dt}(\omega, t)$.

In Tables I and II the values of R_M and R_{dt} are given. These values are obtained by running the test computations with the initial data (34) until $t = 100$ and 50 , respectively. We can state from these results that the rate of convergence with respect to the time step is close to 2, which strictly corresponds to the theoretical estimates of the error of RK2. The convergence with respect to the number of nodes of the spatial grids is exponential, which also agrees with theoretical predictions and with the data from [13].

The described results are obtained for the times $t = 100$ and 50 , which are rather far from the time $t^* \approx 126.7$ at which the solution of the WKE blows up. For the times close to t^* , most of the approximations to the solution fail. Let us finalize our research by studying the convergence of the numerical solutions of the WKE and the conservation of the invariants, namely the density of particles and of energy, in the vicinity of t^* .

To perform this study, we expanded the segment $[\omega_{\min}, \omega_{\max}]$ to $[0.001, 100^2]$, we started with initial data (34), and we ran the computations with $M = 256$ and with manual adaptation of dt until $t = t_0 \approx 124.14$. The adaptation is done in order to decrease the relative deviations of invariants from their initial values as much as possible. At the point $t = t_0$, the deviations start to grow rapidly, and we use the solution at $t = t_0$ as an initial data for our analysis.

TABLE IV. Values of $R_M(n)$ obtained with the fixed step $dt = 0.08$ at various times close to t^* .

M	$t \approx 124.22$	$t \approx 124.7$	$t \approx 125.18$	$t \approx 125.74$
64	0.0199	0.1365	0.2592	0.4343
128	0.0199	0.1316	0.2036	0.2677
256	0.0155	0.1007	0.1982	0.3543
512	0.0046	0.0365	0.0483	0.1458

First, we analyze the convergence with respect to the time step by observing the values of $R_{dt}(n)$ for the fixed $M = 256$ at $t \approx 125.7$. From the data in Table III one can see that the impact of the time-stepping error is rather small, and the order of convergence corresponds to a theoretical value.

Second, we consider the convergence of approximations in a ω -variable. In Table IV the values of $R_M(n)$ computed for $\omega \in [0.1^2, 86^2]$ are given for different M . The time step is fixed, $dt = 0.08$. In this experiment, we are focused on growth of the error in the vicinity of blow-up time. Therefore, we observe several time moments close to t^* .

For the numerical values of spectra obtained in the case $M = 1024$, we compute the relative deviations of the particle and energy densities from their initial values. They are denoted by $D_N(t)$ and $D_H(t)$, respectively, and are presented in Table V. Their formulas are

$$D_N(t) = \frac{N(t) - N(0)}{N(0)}, \quad D_H(t) = \frac{H(t) - H(0)}{H(0)},$$

where $N(t)$ and $H(t)$ are computed by substituting the numerical solution of the WKE obtained for the time moment t into (15) and (16).

From the presented results one can conclude that the error of the numerical solution grows rapidly in the vicinity of blow-up time, and even the usage of rational approximations with a huge number of nodes does not allow us to come very close to t^* . The last more or less adequate approximation of the solution can be obtained at $t \approx 125.7$. The possible reason is that we used rational approximations only for the spectrum, not for the integrands of the collision terms, which obviously also have strong singularities in the vicinity of t^* . Further developments will be directed to the design of new cubature formulas aimed at overcoming this drawback.

An interesting fact is that rather large deviations of the numerical solutions reported in the last column of Table IV do not affect the conservation of invariants very much. In simulation with $M = 1024$, the value of $|D_N|$ jumps a bit to the order of 10^{-4} , and $|D_H|$ remains practically unchanged. The reason is that the largest deviations of numerical solutions in tests with different M , and hence the errors, are localized in the vicinity of the point ω_{\min} , whereas in all other points of the domain $[\omega_{\min}, \omega_{\max}]$ they remain relatively small. For example, a comparison of the 512 and 1024 results on the segment $[1, \omega_{\max}]$ gives a relative deviation of less than 10^{-3} .

TABLE V. Relative deviation of $D_N(t)$ and $D_H(t)$ at various times close to t^* obtained in computations with $M = 1024$, $dt = 0.08$.

	$t \approx 124.22$	$t \approx 124.7$	$t \approx 125.18$	125.74
$D_N(t)$	8.69×10^{-5}	7.61×10^{-5}	3.88×10^{-5}	-3.705×10^{-4}
$D_H(t)$	-1.86×10^{-4}	-1.96×10^{-4}	-2.12×10^{-4}	-1.87×10^{-4}

While comparing the nonconservation of particle and energy densities, one should keep in mind the definitions (15) and (16). Due to the factor $\omega^{1/2}$ in (15), the density of particles

is more sensitive to the error of the spectrum in the vicinity of ω_{\min} than the density of energy. That is why for the times close to t^* , the deviation $D_N(t)$ starts to grow first.

-
- [1] S. Nazarenko, *Wave Turbulence* (Springer Science & Business Media, Heidelberg, 2011), Vol. 825
- [2] V. E. Zakharov, V. S. Lvov, and G. Falkovich, *Kolmogorov Spectra of Turbulence I: Wave Turbulence*, Springer Series in Nonlinear Dynamics (Springer, Berlin, Heidelberg, 1992).
- [3] S. Dyachenko, A. Newell, A. Pushkarev, and V. Zakharov, Optical turbulence: Weak turbulence, condensates and collapsing filaments in the nonlinear Schrödinger equation, *Physica D* **57**, 96 (1992).
- [4] D. Proment, S. Nazarenko, and M. Onorato, Quantum turbulence cascades in the Gross-Pitaevskii model, *Phys. Rev. A* **80**, 051603(R) (2009).
- [5] D. Proment, S. Nazarenko, and M. Onorato, Sustained turbulence in the three-dimensional gross-pitaevskii model, *Physica D* **241**, 304 (2012).
- [6] N. Navon, A. L. Gaunt, R. P. Smith, and Z. Hadzibabic, Emergence of a turbulent cascade in a quantum gas, *Nature (London)* **539**, 72 (2016).
- [7] N. Navon, C. Eigen, J. Zhang, R. Lopes, A. L. Gaunt, K. Fujimoto, M. Tsubota, R. P. Smith, and Z. Hadzibabic, Synthetic dissipation and cascade fluxes in a turbulent quantum gas, *Science* **366**, 382 (2019).
- [8] D. V. Semikoz and I. I. Tkachev, Kinetics of Bose Condensation, *Phys. Rev. Lett.* **74**, 3093 (1995).
- [9] R. Lacaze, P. Lallemand, Y. Pomeau, and S. Rica, Dynamical formation of a Bose-Einstein condensate, *Physica D* **152-153**, 779 (2001).
- [10] C. Connaughton and Y. Pomeau, Kinetic theory and Bose-Einstein condensation, *C. R. Phys.* **5**, 91 (2004).
- [11] N. Bell, V. Grebenev, S. Medvedev, and S. Nazarenko, Self-similar evolution of Alfvén wave turbulence, *J. Phys. A* **50**, 435501 (2017).
- [12] N. K. Bell and S. V. Nazarenko, Reflected wave solution of Alfvén wave turbulence, *J. Phys. A* **51**, 405501 (2018).
- [13] B. Semisalov, V. Grebenev, S. Medvedev, and S. Nazarenko, Numerical analysis of a self-similar turbulent flow in Bose-Einstein condensates, *Commun. Nonlin. Sci. Numer. Simul.* **102**, 105903 (2021).
- [14] Y. V. Lvov and S. Nazarenko, Noisy spectra, long correlations, and intermittency in wave turbulence, *Phys. Rev. E* **69**, 066608 (2004).
- [15] Y. Choi, Y. V. Lvov, and S. Nazarenko, Probability densities and preservation of randomness in wave turbulence, *Phys. Lett. A* **332**, 230 (2004).
- [16] Y. Choi, Y. V. Lvov, S. Nazarenko, and B. Pokorni, Anomalous probability of large amplitudes in wave turbulence, *Phys. Lett. A* **339**, 361 (2005).
- [17] Y. Choi, Y. V. Lvov, and S. Nazarenko, Joint statistics of amplitudes and phases in wave turbulence, *Physica D* **201**, 121 (2005).
- [18] V. Shrira and S. Nazarenko, *Advances in Wave Turbulence*, World Scientific Series on Nonlinear Science Series A (World Scientific, Singapore, 2013).
- [19] Y. Deng and Z. Hani, Full derivation of the wave kinetic equation, [arXiv:2106.0981](https://arxiv.org/abs/2106.0981).
- [20] M. Tanaka and N. Yokoyama, Numerical verification of the random-phase-and-amplitude formalism of weak turbulence, *Phys. Rev. E* **87**, 062922 (2013).
- [21] Y. Choi, S. Jo, Y.-S. Kwon, and S. Nazarenko, Nonstationary distributions of wave intensities in wave turbulence, *J. Phys. A* **50**, 355502 (2017).
- [22] V. E. Zakharov, A. O. Korotkevich, A. Pushkarev, and D. Resio, Coexistence of Weak and Strong Wave Turbulence in a Swell Propagation, *Phys. Rev. Lett.* **99**, 164501 (2007).
- [23] A. Korotkevich, A. Pushkarev, D. Resio, and V. Zakharov, Numerical verification of the weak turbulent model for swell evolution, *Eur. J. Mech. B Fluids* **27**, 361 (2008).
- [24] A. O. Korotkevich, A. Prokofiev, and V. E. Zakharov, On the dissipation rate of ocean waves due to white capping, *JETP Lett.* **109**, 309 (2019).
- [25] J. Banks, T. Buckmaster, A. Korotkevich, G. Kovačič, and J. Shatah, Direct verification of the kinetic description of wave turbulence, [arXiv:2109.02477](https://arxiv.org/abs/2109.02477).
- [26] L. Pitaevskij and S. Stringari, *Bose-Einstein Condensation*, International Series of Monographs on Physics (Clarendon, Oxford, 2003).
- [27] R. Fjørtoft, On the changes in the spectral distribution of kinetic energy for two-dimensional, nondivergent flow, *Tellus* **5**, 225 (1953).
- [28] V. Zakharov, S. Musher, and A. Rubenchik, Hamiltonian approach to the description of non-linear plasma phenomena, *Phys. Rep.* **129**, 285 (1985).
- [29] D. V. Semikoz and I. I. Tkachev, Condensation of bosons in the kinetic regime, *Phys. Rev. D* **55**, 489 (1997).
- [30] D. Proment, M. Onorato, P. Asinari, and S. Nazarenko, Warm cascade states in a forced-dissipated Boltzmann gas of hard spheres, *Physica D* **241**, 600 (2012).
- [31] D. Gottlieb and S. A. Orszag, *Numerical Analysis of Spectral Methods: Theory and Applications* (SIAM, Philadelphia, 1977).
- [32] M. Frigo and S. G. Johnson, The design and implementation of fftw3, *Proc. IEEE* **93**, 216 (2005).
- [33] G. Krstulovic, A theoretical description of vortex dynamics in superfluids. Kelvin waves, reconnections and particle-vortex interaction, Habilitation à diriger des recherches, Université Côte d'Azur, 2020.
- [34] S. M. Cox and P. C. Matthews, Exponential time differencing for stiff systems, *J. Comput. Phys.* **176**, 430 (2002).
- [35] C. Connaughton, S. Nazarenko, and A. Pushkarev, Discreteness and quaresonances in weak turbulence of capillary waves, *Phys. Rev. E* **63**, 046306 (2001).
- [36] V. Zakharov, A. Korotkevich, A. Pushkarev, and A. Dyachenko, Mesoscopic wave turbulence, *JETP Lett.* **82**, 487 (2005).
- [37] Y. V. Lvov, S. Nazarenko, and B. Pokorni, Discreteness and its effect on water-wave turbulence, *Physica D* **218**, 24 (2006).

- [38] A. I. Dyachenko, A. O. Korotkevich, and V. E. Zakharov, Decay of the monochromatic capillary wave, *J. Expt. Theor. Phys. Lett.* **77**, 477 (2003).
- [39] S. Y. Annenkov and V. I. Shrira, Role of non-resonant interactions in the evolution of nonlinear random water wave fields, *J. Fluid Mech.* **561**, 181 (2006).
- [40] V. S. L'vov and S. Nazarenko, Discrete and mesoscopic regimes of finite-size wave turbulence, *Phys. Rev. E* **82**, 056322 (2010).
- [41] V. Shukla and S. Nazarenko, Non-equilibrium bose-einstein condensation, *Phys. Rev. A* **105**, 033305 (2022).
- [42] C. Connaughton, C. Josserand, A. Picozzi, Y. Pomeau, and S. Rica, Condensation of Classical Nonlinear Waves, *Phys. Rev. Lett.* **95**, 263901 (2005).
- [43] G. Falkovich, Bottleneck phenomenon in developed turbulence, *Phys. Fluids* **6**, 1411 (1994).
- [44] V. Borue and S. A. Orszag, Self-similar decay of three-dimensional homogeneous turbulence with hyperviscosity, *Phys. Rev. E* **51**, R856 (1995).
- [45] C. Cichowlas, P. Bonaiti, F. Debbasch, and M. Brachet, Effective Dissipation and Turbulence in Spectrally Truncated Euler Flows, *Phys. Rev. Lett.* **95**, 264502 (2005).
- [46] G. Krstulovic and M. Brachet, Dispersive Bottleneck Delaying Thermalization of Turbulent Bose-Einstein Condensates, *Phys. Rev. Lett.* **106**, 115303 (2011).
- [47] S. Chibbaro, G. Dematteis, C. Josserand, and L. Rondoni, Wave-turbulence theory of four-wave nonlinear interactions, *Phys. Rev. E* **96**, 021101(R) (2017).
- [48] K. Fujimoto and M. Tsubota, Bogoliubov-wave turbulence in Bose-Einstein condensates, *Phys. Rev. A* **91**, 053620 (2015).
- [49] <http://crimson.oca.eu>.
- [50] M. A. Hossain and M. S. Islam, Generalized composite numerical integration rule over a polygon using Gaussian quadrature, *Dhaka Univ. J. Sci.* **62**, 25 (2014).
- [51] H. E. Salzer, Lagrangian interpolation at the chebyshev points $x_{n,\nu} = \cos(\nu\pi/n)$, $\nu = O(1)n$; some unnoted advantages, *Comput. J.* **15**, 156 (1972).
- [52] R. Baltensperger, J. Berrut, and B. Noël, Exponential convergence of a linear rational interpolant between transformed Chebyshev points, *Math. Comput.* **68**, 1109 (1999).
- [53] T. W. Tee and L. N. Trefethen, A rational spectral collocation method with adaptively transformed chebyshev grid points, *SIAM J. Sci. Comput.* **28**, 1798 (2006).
- [54] H. A. Jafari-Varzaneh and S. M. Hosseini, A new map for the Chebyshev pseudospectral solution of differential equations with large gradients, *Numer. Algorithms* **69**, 95 (2015).
- [55] B. Semisalov and G. Kuzmin, Modification of Fourier approximation for solving boundary value problems having singularities of boundary layer type, *CEUR Workshop Proceedings* **1839** (2017).
- [56] S. Idimeshev, Rational approximation in initial boundary value problems with fronts (in Russian), *Comput. Technol.* **25**, 63 (2020).
- [57] W. M. Gentleman, Implementing Clenshaw-Curtis quadrature, II. computing the cosine transformation, *Commun. ACM* **15**, 343 (1972).